

Article

# High-Fidelity Dynamics Modelling for the Design of a High-Altitude Supersonic Sounding Rocket

Benjamin Milne <sup>1,†</sup>, Sean Samson <sup>1,†</sup>, Robert Carrese <sup>1</sup>, Alessandro Gardi <sup>2,1</sup>  and Roberto Sabatini <sup>2,1,\*</sup> <sup>1</sup> School of Engineering, RMIT University, Melbourne, VIC 3000, Australia<sup>2</sup> Department of Aerospace Engineering, Khalifa University of Science and Technology, Abu Dhabi P.O. Box 12778, United Arab Emirates

\* Correspondence: roberto.sabatini@ku.ac.ae; Tel.: +971-2-312-5656

† These authors contributed equally to this work and shall be considered joint first authors.

**Abstract:** The accurate modelling and simulation of vehicle dynamics is a fundamental prerequisite for the design and experimental flight testing of aerospace vehicles. In the case of high-altitude supersonic sounding rockets, it is critically important to produce realistic trajectory predictions in a representative range of operational and environmental conditions as well as to produce reliable probability distributions of terminal locations. This article proposes a methodology to develop high-fidelity flight dynamics models that accurately capture aeroelastic, turbulence, atmospheric and other effects relevant to sounding rockets. The significance of establishing a high-fidelity model and of addressing such a problem in the context of developing a digital twin are discussed upfront, together with the key tools utilised in the analysis. In addition to state-of-the-art computational methods to determine the aerodynamic forces, moments and mass changes in various flight regimes (including parachute release), a detailed methodology for incorporating the dynamic aeroelastic response of the rocket is presented. The validity of the proposed method is demonstrated through a simulation case study, which utilises data from an existing rocket prototype. Results corroborate the correct implementation of the proposed algorithms and provide foundations for future research on virtual sensing and digital twin for autonomous navigation and guidance.

**Keywords:** rocket design; sounding rocket; multi-physics; rocket dynamics; aeroelasticity; digital twin; aerodynamics; flight dynamics; virtual prototyping; computational fluid dynamics; computational structural mechanics



**Citation:** Milne, B.; Samson, S.; Carrese, R.; Gardi, A.; Sabatini, R. High-Fidelity Dynamics Modelling for the Design of a High-Altitude Supersonic Sounding Rocket. *Designs* **2023**, *7*, 32. <https://doi.org/10.3390/designs7010032>

Academic Editor: Hamid Reza Karimi

Received: 14 October 2022

Revised: 29 January 2023

Accepted: 9 February 2023

Published: 15 February 2023



**Copyright:** © 2023 by the authors. Licensee MDPI, Basel, Switzerland. This article is an open access article distributed under the terms and conditions of the Creative Commons Attribution (CC BY) license (<https://creativecommons.org/licenses/by/4.0/>).

## 1. Introduction

High-fidelity multi-physics models are very instrumental in the design and virtual testing of aerospace vehicles. Accurate dynamics and simulation models are equally important to support the design of the intended aerospace vehicle payload as well as its navigation [1] and guidance [2,3] systems. For instance, realistic flight dynamics models have proven their effectiveness through numerous past studies to compensate for the outages and error spikes of common navigation sensors such as Global Navigation Satellite Systems (GNSSs), strap-down Micro-Electro-Mechanical Inertial Measurement Units (MEMS-IMU) and magnetometers [4,5] and have also been extensively used to inform the design of autonomous integrity monitoring and augmentation systems [6–8]. This article presents a methodology to accurately determine the dynamics model of a sounding rocket also considering its aeroelastic response, which can be used to accomplish an accurate trajectory simulation from the ignition, launch rail motion, boosting phase, coasting phase and recovery phase. At a sufficiently high fidelity, these models allow one to create a digital twin or even a virtual prototype of the physical system, not only supporting the Design, Development Testing and Evaluation (DDT&E) of the vehicle and its systems but also enabling predictive maintenance (diagnosis and prognosis) of the vehicle parts as they undergo wear and tear during use [9]. The digital twin can also support the study and post

hoc assessment of atypical and unforeseen events during flight, for example, the failure of the parachute to deploy. A degree of confidence in the behaviour of the rocket in nominal and off-nominal conditions and in the associated touchdown locations is also required to complete risk assessments and inform new safety standards, relieving some of the most imposing requirements for the evacuation of launch and re-entry sites [10].

High-fidelity dynamics models shall address an appropriate integration of Computational Fluid Dynamics (CFD), Computational Flight Mechanics (CFM) and Computational Structural Dynamics (CSD) to calculate the forces and moments acting on the system at any given point in-flight (Figure 1). These models incorporate the physical phenomena that the rocket will experience during flight, such as atmospheric property changes and turbulence, unsteady aerodynamic forces and moments, thrust variations, parachute forces and change in inertia due to fuel burn.

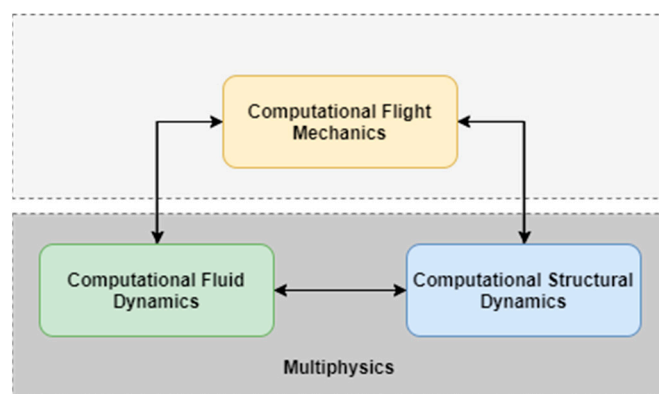


**Figure 1.** Governing subsystem interactions.

The remainder of this section presents a review of the relevant literature. Next, Section 2 outlines the methodology and key models that are incorporated into the analysis, with a focus on the method of determining the aerodynamic forces and moments, and the aeroelastic response of the rocket. These methods are then applied in Section 3 to the Ad Astra II rocket to determine its trajectory under expected conditions and to analyse the deformations occurring in such a scenario due to aeroelastic interactions. Finally, the article concludes with a summary of the findings of this research project and recommendations for future work.

### 1.1. Aerodynamic Coefficient Determination

Central to the development of a high-fidelity dynamics model is the accurate calculation of the rocket's aerodynamic coefficients and stability derivatives as these define the overall response of the vehicle at different angles of attack, sideslip, atmospheric conditions and altitudes. While wind tunnel and range tests [11] have been the predominant methods to estimate a rocket's aerodynamic coefficients, modern tools such as semi-empirical, analytical and CFD methods have also seen widespread use for both rockets [12,13], missiles and launch vehicles [14]. Industry-standard software such as USAF Missile Data Compendium (DATCOM) [15] and Aeroprediction Code [16] in particular has seen extensive use. These methodologies are based on a combination of analytical and empirical methods, which can jointly overcome their limited validity as a function of the Mach regime, flow conditions, angles of attack and components under analysis.

Increasing computing power has supported the prevalence of CFD methods and the direct application of these methods within 6DoF rigid-body flight dynamics simulations has been successfully demonstrated in the literature, also for hypersonic rigid-body motion [17]. Another study using direct CFD/Rigid Body Motion (RBM) interactions focused on a spinning, finned projectile [18]. Real-time rigid-body flight data were simulated through the use of a Reynolds-averaged Navier–Stokes (RANS) flow solver with CFD++ codes, coupling directly with a 6DoF dynamics module to receive the relevant aerodynamic

coefficients of the resultant displacements and rotations to be reapplied to CFD simulation through the manipulation of ‘Chimera’ or ‘overlapping’ grids. This methodology resulted in high agreement with experimental data and, therefore, is ideally suited to calculate flight trajectories considering unsteady aerodynamics. This approach was further developed in [19] where CFD/RBM interactions were additionally coupled with CFD/CSD. This and subsequent studies demonstrated that spin introduces non-negligible inertial coupling modes also in conjunction with induced structural vibrations.

To overcome the still prohibitive computational costs involved in the direct integration of the RANS model in full-size trajectory simulations, alternative approaches in the literature implemented linearly interpolated look-up tables as in [13]. This methodology, however, runs the risk of correlating poorly within flow regimes dominated by non-linear aerodynamics. Thus, the application within large time-scale trajectory simulations requires alternative methodologies, particularly where more complex and coupled CFD/CSD/CSM simulations are needed such as in the aeroelastic analysis.

Table 1 summarizes the findings of the literature review on aerodynamic coefficient determination methods by comparing the various approaches discussed in this section and their respective advantages and disadvantages.

**Table 1.** Comparison of rigid-body aerodynamic coefficient calculation methods.

Method	Pros	Cons
Direct CFD Calculation	<ul style="list-style-type: none"> <li>- Any rocket configuration can be calculated.</li> </ul>	<ul style="list-style-type: none"> <li>- High computational intensity prevents direct usage for real-time simulations.</li> </ul>
Look Up Table Development using CFD Calculation	<ul style="list-style-type: none"> <li>- Any rocket configuration can be calculated.</li> <li>- After data are generated, it will enable the rapid interpolation of aerodynamic coefficients within the dynamics model.</li> </ul>	<ul style="list-style-type: none"> <li>- Interpolation methods may not provide accurate enough information.</li> <li>- With a scope of trajectory simulation, parameters such as angle of attack, sideslip, Mach number and other flow characteristics would require alteration to enable an adequate data set.</li> </ul>
Semi-Empirical and Analytical Calculation	<ul style="list-style-type: none"> <li>- Rapid calculation of coefficients and stability derivatives.</li> <li>- Geometrically defined characteristics allow for continuously updating calculations.</li> </ul>	<ul style="list-style-type: none"> <li>- Without corrections, it only calculates characteristics for low angles-of-attack.</li> <li>- Cannot directly calculate in the transonic region.</li> <li>- Supersonic assumptions include a sharp nose and straight and tapered fins.</li> </ul>

### 1.2. Aeroelastic Modelling

Aeroelastic phenomena impact the lift, drag, moment coefficients and stability of the rocket and have become a major consideration for increasing the slenderness factors and control forces [20]. For instance, high-Mach number testing campaigns in the 1950s found that large aerostructural deformations could lead to inaccurate results or failure of the model-booster combination [21]. In more recent periods, aeroelastic analysis has grown in importance for modern gas turbomachinery; however, in this application, it is possible to rely on potential flow theory through many assumptions and approximations [22], which are not valid for rocket bodies.

One of the most common avenues for aeroelastic modelling is to use coupled fluid-mechanical solvers in order to solve for the steady-state aeroelastic aerodynamic coefficients and deformation. This method is used in [23] for slender spinning missiles, showing that a one-way coupled method is insufficient to accurately capture the effects of aeroelastic deformation at larger angles of attack.

A promising approach to overcome the still high computational costs of coupled CFD/CSD methods is surrogate modelling, which can rely on a neural network trained using CFD data to ‘learn’ the behaviour of the body being studied. A surrogate modelling technique based on a Radial Basis Function (RBF) Artificial Neural Network (ANN) is used in [24] to reproduce non-linear aerodynamic effects under high Reynolds’ Number conditions. In this study, a reduced-order model (ROM) is generated for a 3D wing structure

with both a static and transient aeroelastic case. After 255 CPU hours of training on the static case and 6961 h of training on the transient case, the ROM was able to accurately model the deformation and aerodynamic loads experienced by the wing.

An alternative is to undertake a modal analysis of the static Euler bending modes, as in [25], where the impact of the different bending modes on the static aeroelastic deformation of a slender rocket is studied. This method allows one to create a linear reduced-order modal approximation of the bending characteristics as an alternative to more computationally expensive finite-element methods (FEMs). In that study, the static aeroelastic bending was found to be dominated by the first two bending modes, and bending modes above the 6th order were found to play a negligible role in the static deformation of the rocket.

The Modal Projection and Force Reconstruction (MPR) is also based on modal analysis with a two-way fluid-structural interface (FSI) force allocation [26]. This method is highly accurate, achieving results within 0.6% error for the vertical displacement of a beam.

The Nonlinear Strip Method (NSM), on the other hand, solves the nonlinear aerodynamic effects using a database of rigid force coefficients [27]. This method discretises the outer structure of the rocket into strips, calculates the deformed angle of attack using a static CFD model and a database and then iterates the new aerodynamic forces due to the deformed angle of attack. This method was found to be significantly more computationally efficient than a full nonlinear aeroelastic analysis while maintaining high fidelity—it predicted aerodynamic effects to within 10% of traditional aeroelastic methods [27].

### 1.3. Atmospheric Properties and Disturbance Modelling

Critical to the development of a high-fidelity 6DoF trajectory simulation is the accurate modelling of relevant atmospheric properties and disturbances as these all affect the unsteady flight dynamics during flight. Non-standard models have traditionally been implemented using MIL-HDBK-310 [28], which introduces climactic variations in how atmospheric conditions are calculated. Local disturbances, on the other hand, significantly influence the performance and handling qualities of all aerospace vehicles, and their consideration within the design, evaluation and certification of civil and military aircraft have been well documented. Wu, et al. [29] provide a comprehensive evaluation of prevalent and emerging gust models related to vehicle performance. Existing gust models are largely categorised as either discrete, continuous or statistically discrete in nature. Discrete gusts are employed for the investigation of performance in the event of a large, static load. These come in the various forms of step, linear-ramp and ‘1-cosine’ gust velocity distributions. In the event that more random disturbances and structural analyses of the aircraft are being investigated, continuous stochastic models are implemented. The most common are the Dryden and von Karman power-spectra models. Where continuous gusts implicate a Gaussian or ‘normal’ distribution that results in a more ‘real-world’ model, Statistical Discrete Gust (SDG) models implement a non-Gaussian, worst-case model, where a highly damped aircraft can exhibit a response.

While British regulations implement SDGs as part of their airworthiness evaluation, regulations such as FAR-25, MIL-F-8785C and MIL-HDBK-1797 favour the implementation of a combination of discrete and continuous models. For the evaluation of aircraft handling qualities and control performance in particular, both MIL-F-8785C and MIL-HDBK-1797 prescribe the parallel implementation of at least the 1-cosine discrete gust model and, ideally, the von Karman continuous turbulence model [30,31]. This is typically due to the observed atmospheric data supporting both.

Not dissimilar to modern vehicle aerodynamic characteristic calculations, CFD methods have also seen use within the investigation of vehicle behaviour in atmospheric disturbances. Reimer, et al. [32] demonstrate a high-fidelity, but highly computationally intensive CFD approach to gust modelling using a RANS-based solver to model the application of a 1-cosine gust on an aircraft. This implementation allows for the simulation of CFD-CSD modelling to analyse the aircraft’s accurate response. Where a rapid analysis of many different gust conditions is required, the application of ROMs in the form of Proper Orthogonal

Decomposition (POD) has also been demonstrated to accurately simulate discrete gust disturbances on an aircraft with minimal error [33].

During the development of the Space Shuttle, there was a need for a more realistic representation of high-altitude turbulence. A new model was needed to allow for the accurate estimation of the Reaction Control System (RCS) fuel usage due to the turbulence model being implemented assuming severe turbulence throughout the whole flight. Justus et al. [34], therefore, developed a methodology that implemented a more realistic turbulence model which used a stochastic turbulent intensity model with the capability to model gusts up to 200 km in altitude. This program has now developed into the NASA Earth Global Reference Atmospheric Model that continues to implement a robust gust modelling functionality, paired with a comprehensive array of supplementary information about historical climactic data worldwide [35].

#### *1.4. Recovery Methods and Parachute Modelling*

An important phase of the trajectory of a sounding rocket is its descent and recovery, where the forces and moments produced by the parachutes, including during their deployment, have a massive impact on the 6DoF dynamics of the vehicle. Similar to the case of aeroelastic analysis, the most rigorous yet computationally expensive approach for parachute inflation modelling is CFD. Because of this, much of the research on high-performance parachutes, especially in earlier periods, involved fitting empirical functions to flight test data taken on sled tests, rocket tests and aircraft drop tests to predict the drag of the parachute and its filling time [36]. These models have been validated up to Mach 2.2; however, due to the relatively simple nature of these models, the error margins for the functions remain high.

Arbitrary Lagrangian–Eulerian (ALE) CFD methods, on the other hand, can model the permeability of the parachute fabric to more accurately solve for the drag force [37]; however, they are severely limited by computational costs. A compromise is to use ALE for the inflation portion of the flight, but then to use traditional CFD models for the steady-state response [37].

Incorporating parachute models into a 6DoF trajectory analysis also presents a challenge due to unpredictable atmospheric characteristics. A possible approach is to perform a Monte Carlo analysis to find the dispersion due to uncertainties in aerodynamic coefficients, atmospheric characteristics and the flight parameters at the start of the re-entry [38]. This study, however, produced instability in the angle of attack. An alternative method for finding the trajectory of a parachute is to simplify the equations of motion to use a simple 3DoF model. While this method is significantly simpler than a full 6DoF model, it was found that it is accurate to within engineering tolerances for most applications [39].

#### *1.5. Model Verification*

Uncertainties can be found in the integration of design tolerances within the components, variations in the initial conditions or environmental conditions such as wind direction and intensity. In many studies, these uncertainties have been considered by adopting nominally deterministic dynamics functions using Monte Carlo Simulation (MCS) [40]. For instance, MCS can be used to model the effects of turbulence and gusts on the final touchdown location of a rocket [12,13]. However, MCS as a random sampling method requires a very large number of samples to adequately capture the uncertainty and robustness associated with a variety of linear and nonlinear effects. Recent studies have, therefore, seen the application of different random sampling methods aiming for a more robust and less computationally expensive characterization of uncertainties. For instance, Eerland et al. [41] noted that the application of MCS can result in probabilistic output distributions containing unrepresentative, low-probability outcomes that overall contribute to invalidating the probability distribution, instead opting for the use of a Gaussian process to obtain more representative outcomes. On the other hand, Refs [14,41,42] focussed on an Improved Latin Hypercube Sampling (ILHS), which resulted in better-filled sample spaces.

## 2. Materials and Methods

This section describes the methodology that was implemented for the high-fidelity modelling and simulation of sounding rocket flight dynamics, comprehensive of each factor considered and how these interact, as well as the assumptions and approximations.

This section starts by introducing the frames of reference and all the models, such as the 6DoF equations of motion, atmospheric and turbulence, aerodynamic loads, parachute and thrust. Subsequently, the methodology used to calculate the aeroelastic response of the rocket due to aerodynamic loads and its structural response and the methods used to calculate the touchdown location using a statistical distribution are presented. Figure 2 outlines the overall model determination process.

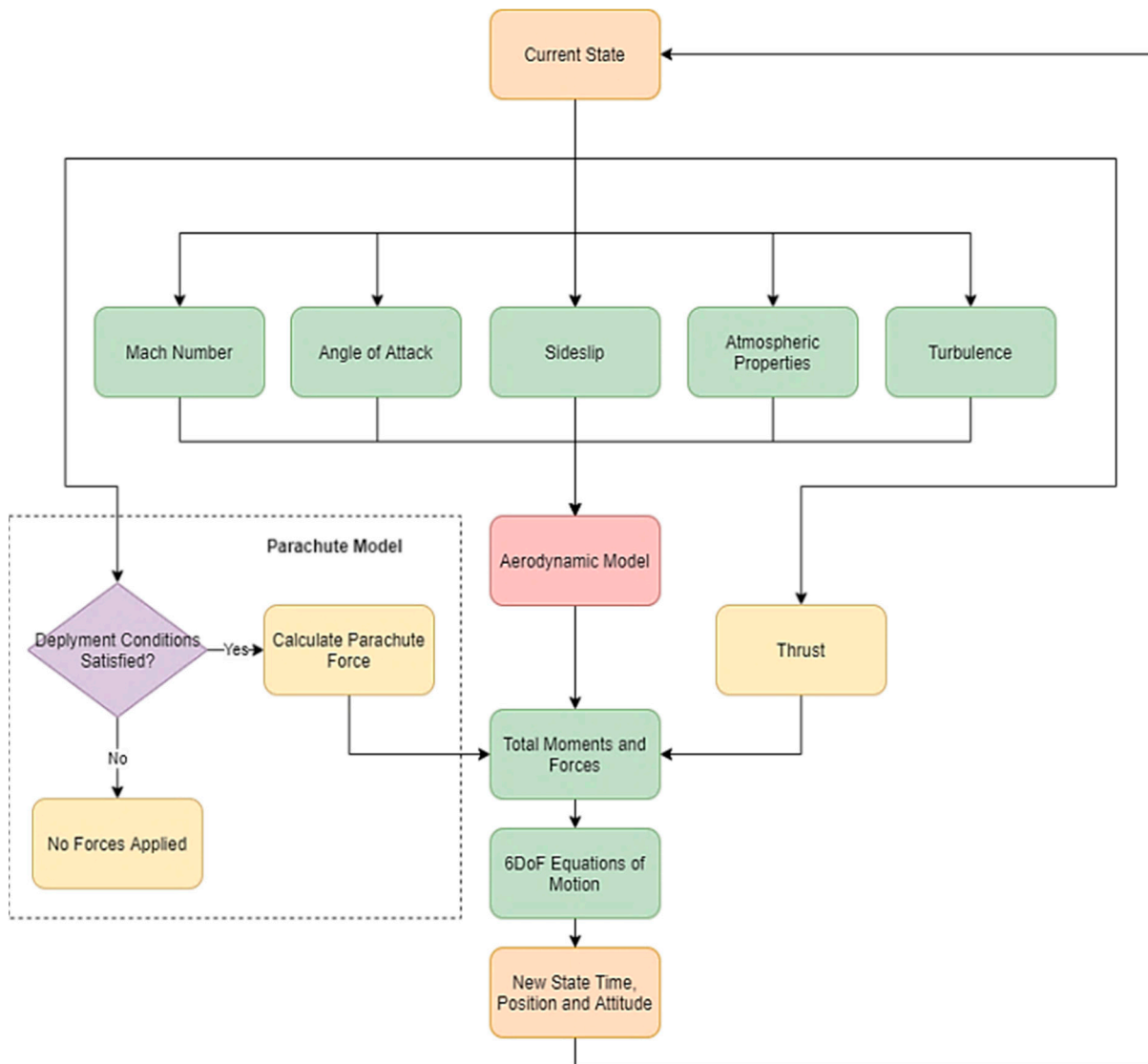


**Figure 2.** Flowchart of the overall model determination process.

After calculating the properties of the current state of the rocket, a CFD-based aerodynamic model is used to calculate the aerodynamic forces and moments acting on the body. Next, the additional forces and moments due to the thrust and the parachute model are applied to find the total forces and moments acting upon it. Finally, these forces are integrated using the 6DoF equations of motion to find the next state of the rocket.

2.1. Frames of Reference, Equations of Motion and Numerical Integration

Within this dynamics model, the body frame of reference has been oriented in accordance with the traditional right-hand rule; where the x-axis is oriented towards the nose, the y-axis is oriented towards the starboard side of the rocket, and the z-axis is oriented downwards (Figure 3).

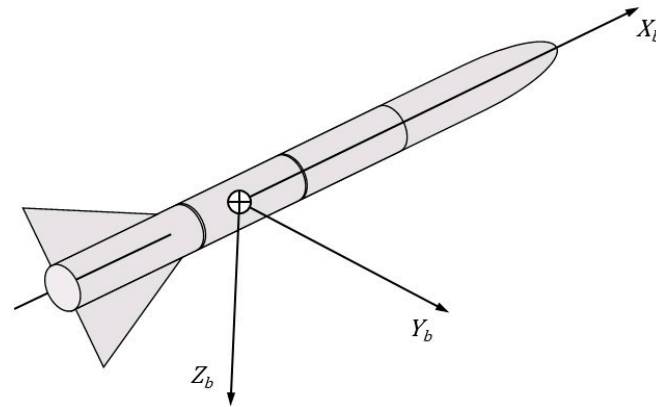


Figure 3. Adopted rocket body axes reference frame.

For the inertial frame, we resort to a spherical Earth-Centred-Earth-Fixed (ECEF) frame of reference (Figure 4), with positions expressed in latitude, longitude and altitude components. Finally, the local north–east–down (NED) cartesian coordinate system is chosen as the navigational (auxiliary) frame of reference.

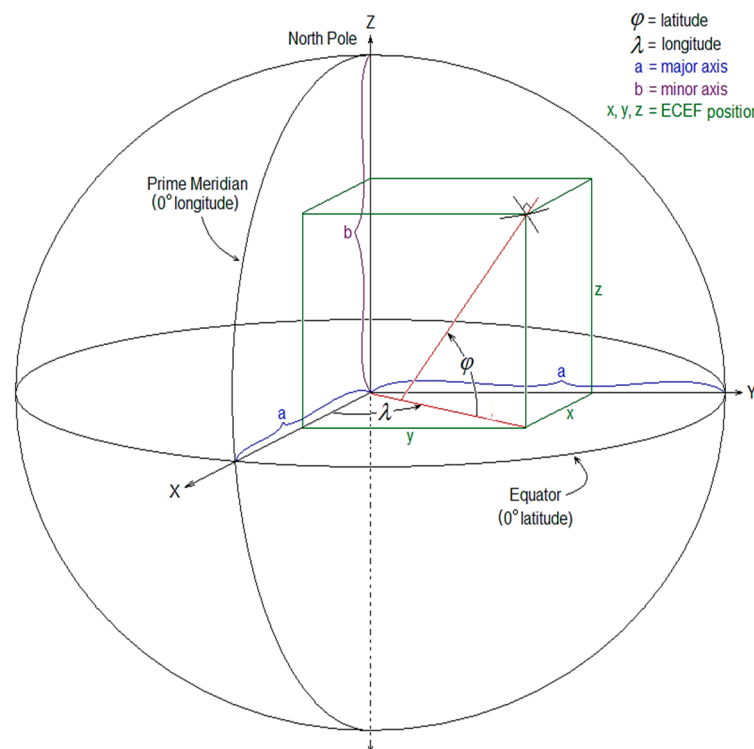


Figure 4. Adopted ECEF coordinate system [43].

The position, velocity and acceleration of a body about the individual translational and rotational directions are derived from Newton’s Second Law. These equations for a general case are presented below.

For the translational frame, the velocity of the body in the  $x_b$ ,  $y_b$  and  $z_b$  axes is given by:

$$v_b = \begin{bmatrix} u \\ v \\ w \end{bmatrix} \tag{1}$$

With thrust ( $T$ ), lift ( $L$ ) and drag ( $D$ ) acting through the centre of gravity of the rocket, we can find the forces acting on the body.

$$F_b = \begin{bmatrix} X \\ Y \\ Z \end{bmatrix} = \begin{bmatrix} -D\cos(\alpha) + L\sin(\alpha) + T\cos(\phi_T) \\ F_{aero,y} \\ -D\sin(\alpha) - L\cos(\alpha) - T\sin(\phi_T) \end{bmatrix} \tag{2}$$

The rate of change of the translational position is given by:

$$\begin{aligned} \dot{x}_I &= u \cos \theta \cos \psi + (-\cos \phi \sin \psi + \sin \phi \sin \theta \cos \psi)v \\ &\quad + (\sin \phi \sin \psi + \cos \phi \sin \theta \cos \psi)w \\ \dot{y}_I &= u \cos \theta \sin \psi + (\cos \phi \cos \psi + \sin \phi \sin \theta \sin \psi)v \\ &\quad + (-\sin \phi \cos \psi + \cos \phi \sin \theta \sin \psi)w \\ \dot{z}_I &= -u \sin \theta + v \sin \phi \cos \theta + w \cos \phi \cos \theta \end{aligned} \tag{3}$$

where  $\phi$ ,  $\theta$  and  $\psi$  represent Euler angles. Finally, the rate of change of translational position is given by the following equations:

$$\begin{aligned} \dot{u} &= \frac{X}{m} - g \sin \theta + rv - qw \\ \dot{v} &= \frac{Y}{m} + g \sin \phi \cos \theta + ru + pw \\ \dot{w} &= \frac{Z}{m} + g \cos \phi \cos \theta + qu - pv \end{aligned} \tag{4}$$

where  $p$ ,  $q$  and  $r$  are the rotational velocities in the  $x$ ,  $y$  and  $z$  body axes. The rotational velocities and accelerations are found using a similar method.

In the case of sounding rockets, the vehicle can potentially reach and exceed 90 degrees of pitch, resulting in an ambiguity of the equations (and the associated phenomenon of ‘gimbal lock’ in real systems). To prevent this mathematical singularity within the dynamics model, the quaternion representation has been adopted following Siouris [44]. This is applied with a direct cosine matrix, transforming the body velocities calculated into inertial velocities, which is constructed using the Euler angles and quaternions parameters:

$$v_b = C_q v_i \tag{5}$$

where:

$$C_q = \begin{bmatrix} A^2 - B^2 - C^2 + D^2 & 2(AB - CD) & 2(AC + BD) \\ 2(AB + CD) & -A^2 + B^2 - C^2 + D^2 & 2(BC - AD) \\ 2(AC - BD) & 2(BC + AD) & -A^2 - B^2 + C^2 + D^2 \end{bmatrix} \tag{6}$$

where  $A$ ,  $B$ ,  $C$  and  $D$  are calculated as the following:

$$\begin{aligned} A &= \sin\left(\frac{\psi}{2}\right) \sin\left(\frac{\theta}{2}\right) \cos\left(\frac{\phi}{2}\right) - \cos\left(\frac{\psi}{2}\right) \cos\left(\frac{\theta}{2}\right) \sin\left(\frac{\phi}{2}\right) \\ B &= -\cos\left(\frac{\psi}{2}\right) \sin\left(\frac{\theta}{2}\right) \cos\left(\frac{\phi}{2}\right) - \sin\left(\frac{\psi}{2}\right) \cos\left(\frac{\theta}{2}\right) \sin\left(\frac{\phi}{2}\right) \\ C &= -\sin\left(\frac{\psi}{2}\right) \cos\left(\frac{\theta}{2}\right) \cos\left(\frac{\phi}{2}\right) + \cos\left(\frac{\psi}{2}\right) \sin\left(\frac{\theta}{2}\right) \sin\left(\frac{\phi}{2}\right) \\ D &= -\cos\left(\frac{\psi}{2}\right) \cos\left(\frac{\theta}{2}\right) \cos\left(\frac{\phi}{2}\right) - \sin\left(\frac{\psi}{2}\right) \sin\left(\frac{\theta}{2}\right) \sin\left(\frac{\phi}{2}\right) \end{aligned} \tag{7}$$

Once the forces and moments are determined in each axis, they are integrated to find the position, velocity and acceleration at the next time step. In addition to implementing the quaternion representation, this model considers the reduction in mass of the rocket due to burning fuel by assuming a linear change in the mass moment of inertia from the

full mass to the empty mass. The integration technique used is a 4th order Runge–Kutta method, detailed below:

$$\begin{aligned}
 K_1 &= hf(x_n, y_n) \\
 K_2 &= hf\left(x_n + \frac{h}{2}, y_n + \frac{k_1}{2}\right) \\
 K_3 &= hf\left(x_n + \frac{h}{2}, y_n + \frac{k_2}{2}\right) \\
 K_4 &= hf(x_n + h, y_n + k_3) \\
 y_{n+1} &= y_n + \frac{k_1}{6} + \frac{k_2}{3} + \frac{k_3}{3} + \frac{k_4}{6}
 \end{aligned}
 \tag{8}$$

This method is included in Matlab/Simulink as the ODE45 method and was chosen due to its large region of stability over more simple integration techniques as well as its high accuracy.

### 2.2. Atmospheric and Turbulence Models

The atmospheric model implemented within the current dynamics model is that of the (COESA-extended) U.S. Standard Atmosphere Model as it has been implemented within Simulink. While this affords the model simple tuning to convert the model block to output conditions representing that of MIL-HDBK-310, the handbook showcases the general environmental conditions globally. Hypothetical launches within Victoria can be modelled using the U.S. Standard Atmosphere, and future HIVE launches near Queensland can potentially be modelled using the high-temperature extreme condition. This is of course subject to the season and approximate weather on the hypothetical day of launch.

The preliminary implementation of the discrete and continuous gust models has been through the manipulation of the body-fixed frame velocity. In accordance with standard MIL-HDBK-1797A, the discrete 1-cosine gust is mathematically represented by the following [31]:

$$V_{wind} = \begin{cases} 0 & x < 0 \\ \frac{V_m}{2} \left[ 1 - \cos\left(\frac{\pi x}{d_m}\right) \right] & 0 \leq x \leq d_m \\ V_m & x > d_m \end{cases}
 \tag{9}$$

where  $V_m$  is the amplitude of the gust and  $d_m$  is the gust length.

To maintain consistency with the above standards, the continuous von Karman turbulence model is represented mathematically by the following Power-Spectral Density (PSD) functions for continuous gusts in the longitudinal, lateral and vertical directions relative to the rocket body to calculate both induced velocities ( $u, v, w$ ) and rotational rates ( $p, q, r$ ):

$$\Phi_u(\omega) = \frac{2\sigma_u^2 L_u}{\pi V} \cdot \frac{1}{\left[ 1 + \left( \frac{1.339 L_u \omega}{V} \right)^2 \right]^{\frac{5}{6}}}
 \tag{10}$$

$$\Phi_p(\omega) = \frac{\sigma_w^2}{VL\omega} \cdot \frac{0.8 \left( \frac{\pi L_w}{4b} \right)^{\frac{1}{3}}}{1 + \left( \frac{4b\omega}{\pi V} \right)^2}
 \tag{11}$$

$$\Phi_v(\omega) = \frac{\sigma_v^2 L_v}{\pi V} \cdot \frac{1 + \frac{8}{3} \left( \frac{1.339 L_v \omega}{V} \right)^2}{\left[ 1 + \left( \frac{1.339 L_v \omega}{V} \right)^2 \right]}
 \tag{12}$$

$$\Phi_r(\omega) = \frac{\mp \left( \frac{\omega}{V} \right)^2}{1 + \left( \frac{3b\omega}{\pi V} \right)^2} \cdot \Phi_v(\omega)
 \tag{13}$$

$$\Phi_w(\omega) = \frac{\sigma_w^2 L_w}{\pi V} \cdot \frac{1 + \frac{8}{3} \left( \frac{1.339 L_w \omega}{V} \right)^2}{\left[ 1 + \left( \frac{1.339 L_w \omega}{V} \right)^2 \right]} \tag{14}$$

$$\Phi_q(\omega) = \frac{\mp \left( \frac{\omega}{V} \right)^2}{1 + \left( \frac{4b\omega}{\pi V} \right)^2} \cdot \Phi_w(\omega) \tag{15}$$

where  $\Phi$  is the power-spectral density,  $\sigma$  is the RMS gust velocity,  $\omega$  is the frequency and  $L$  are the length scales in each along each respective axis. Equations (19) and (21) allow for the discretionary selection of which direction the lateral and vertical rotational rates are applied to the rocket. In this case, positive lateral and vertical angle rates were selected. As these rates act within the body-fixed frame of reference, the body-fixed velocities and the current altitude of the rocket need to be sourced from the 6DoF equations of motion, as well as the transposed  $DCM_{ned}$ . The resulting turbulence velocities and rotational rates are then added to the rocket’s body-fixed velocities whereby the next time step within the model is calculated. This is applied throughout the duration of the launch.

### 2.3. Aerodynamics Models

Based on the considerations discussed in Section 1.1, to calculate all the necessary aerodynamic coefficients throughout the rocket’s flight while maintaining high modelling accuracy, it was elected to run a series of CFD studies in a carefully defined set of representative conditions, and successively allow the coupled FSI analysis to interpolate (but not extrapolate) the response between calculated values in the obtained look-up table. This practice is in line with the majority of studies not specifically tackling the aerodynamic transients or flutter phenomena.

#### 2.3.1. CFD Modelling

A CFD-based model is used to calculate the aerodynamic forces and moments produced by the rocket during flight. The enclosure sizing is sized using the relationship described in [25] using a cylindrical enclosure with a distance of 5 times the rocket diameter (5D) to the inlet, 15D laterally and 30D to the outlet downstream. In order to find an appropriate mesh resolution for the CFD model, a mesh sensitivity study was conducted. The study was conducted at an angle of attack of 0 degrees and at standard sea level conditions of pressure and density being 101,325 Pa and 1.225 kg/m<sup>3</sup>, respectively. In addition, the viscosity of the fluid varies with the Sutherland three coefficient formula, and the turbulence model used is the SST k-omega model.

The SST k-omega model combines the k-omega model and the k-epsilon turbulence models, which simulate the flow regions close to the wall and away from the wall, respectively [45]. The SST k-omega model is governed by the following equations. First, the turbulent kinetic energy equation is given by:

$$\frac{\partial k}{\partial t} + U_j \frac{\partial k}{\partial x_j} = P_k - \beta^* k \omega + \frac{\partial}{\partial x_j} \left[ (v + \sigma_k v_T) \frac{\partial k}{\partial x_j} \right] \tag{16}$$

With a specific dissipation rate calculated by:

$$\frac{\partial \omega}{\partial t} + U_j \frac{\partial \omega}{\partial x_j} = a S^2 - \beta^* \omega + \frac{\partial}{\partial x_j} \left[ (v + \sigma_\omega v_T) \frac{\partial \omega}{\partial x_j} \right] + 2(1 - F_1) \sigma_{\omega 2} \frac{1}{\omega} \frac{\partial k}{\partial x_i} \frac{\partial \omega}{\partial x_i} \tag{17}$$

The first blending function is given by:

$$F_1 = \tanh \left\{ \min \left[ \max \left( \frac{\sqrt{k}}{\beta^* \omega y}, \frac{500v}{y^2 \omega} \right), \frac{4\sigma_{\omega 2} k}{CD_{k\omega} y^2} \right] \right\}^4 \tag{18}$$

where  $CD_{k\omega} = \max\left(2\rho\sigma\omega^2\frac{1}{\omega}\frac{\partial k}{\partial x_i}\frac{\partial \omega}{\partial x_i}, 10^{-10}\right)$ . Next, the kinematic eddy viscosity is calculated by:

$$v_T = \frac{a_1 k}{\max(a_1\omega, SF_2)} \tag{19}$$

The second blending function is then given by:

$$F_2 = \tanh\left[\max\left(\frac{2\sqrt{k}}{\beta^*\omega y}, \frac{500v}{y^2\omega}\right)\right]^2 \tag{20}$$

Finally, the production limiter is found with the equation:

$$P_k = \min\left(\tau_{ij}\frac{\partial U_i}{\partial x_j}, 10\beta^*k\omega\right) \tag{21}$$

### 2.3.2. Calculation of Aerodynamic Coefficients and Derivatives

The CFD analysis, which in our case was carried out in ANSYS FLUENT, allows one to determine the lift, drag and normal coefficients, as well as the moment coefficients about a centre of gravity. A mesh sensitivity analysis is to be completed upfront to validate the CFD results. As this is standard practice in the domain, no extensive description is provided here, but the interested reader is advised to refer to Section 3.1, as part of the verification case study, further down the article for additional information. This section, therefore, details how coefficients are determined by summing the pressure forces on the face of each cell of the rocket and dividing by the dynamic pressure. In order to find the coefficient in direction  $j$ , the force is found by multiplying the pressure on cell  $i$  by the area of that cell in the  $i$ -direction.

$$C_j = \frac{\sum_{i=1}^N P_i A_{ji}}{\frac{1}{2}\rho v^2 S} \tag{22}$$

For this rocket, the reference area  $S$  is the area of the rocket tube. The moment coefficients were calculated about 16 possible centres of gravity, allowing us to determine the change in the moment due to the burning of solid fuel and the associated movement of the centre of gravity.

The aerodynamic derivatives are derived from the forces and moments by studying their variation as a function of a single independent variable. For instance, to find the derivative of lift with respect to the angle of attack between two points, the following equation is used:

$$\frac{dC_L}{d\alpha} = \frac{C_{L2} - C_{L1}}{\alpha_2 - \alpha_1} \tag{23}$$

These derivatives are found with respect to each variable of interest, and this is how the CFD modelling is incorporated into the Simulink trajectory simulation. With the coefficients and derivatives known, these can be used to linearly interpolate between collected points of data to estimate data within the different combinations of incidence angles and Mach numbers. This is organised into arrays—2D for the force coefficients and 3D arrays for the moment coefficients—to account for the additional change due to a change in rocket mass. The process to interpolate instantaneous coefficient values can be seen below. Let  $C_{xij}$  be an instantaneous value to determine.  $x$  may be an axial, normal or side force coefficient of the rocket in the body frame.  $i$  and  $j$  are the instantaneous incidence angle (angle of attack or sideslip) and the Mach number.  $C_x$  is the corresponding coefficient database with the format of:

$$C_{xmn} = \begin{bmatrix} C_{x11} & C_{x12} & \dots & C_{x1n} \\ C_{x21} & C_{x22} & & \vdots \\ \vdots & & \ddots & \vdots \\ C_{xm1} & \dots & \dots & C_{xmn} \end{bmatrix} \tag{24}$$

where  $m$  and  $n$  are the number of incidence angles and Mach number data points available, respectively.

The first step is to interpolate a column of data that represent the different incidence angles available for the Mach  $j$ , which is calculated using the following.

$$C_{x_{mj}} = C_{x_{n_{lower}}} + \frac{M_j - M_{lower}}{M_{upper} - M_{lower}} (C_{x_{n_{upper}}} - C_{x_{n_{lower}}}) \tag{25}$$

where:

$$C_{x_{mj}} = \begin{bmatrix} C_{x1j} \\ C_{x2j} \\ \vdots \\ C_{x_{mj}} \end{bmatrix}$$

The lower and upper subscripts are the column value or column vectors containing the closest set of data above and below the instantaneous Mach number, respectively. The final interpolation for the instantaneous incidence angle can be calculated in a similar way to determine the final coefficient value.

$$C_{x_{ij}} = C_{x_{m_{lower}}} + \frac{\alpha_i - \alpha_{lower}}{\alpha_{upper} - \alpha_{lower}} (C_{x_{m_{upper}}} - C_{x_{m_{lower}}}) \tag{26}$$

where upper and lower refer to the likewise angles above and below the instantaneous angle. This results in the final force coefficient  $C_{x_{ij}}$ . Moment coefficients are calculated similarly; however, due to the mass variation during flight, an additional interpolation needs to be completed at the start to interpolate the instantaneous mass  $k$ . The moment coefficient database hosts an additional dimension of length  $o$  which is the number of different mass data points considered in the creation of the database.

$$C_{x_{mk}} = C_{x_{m_{lower}}} + \frac{m_k - m_{lower}}{m_{upper} - m_{lower}} (C_{x_{o_{upper}}} - C_{x_{o_{lower}}}) \tag{27}$$

where the upper and lower subscripts once again refer to the closest arrays of masses above and below the instantaneous mass of the rocket, respectively. The procedure from then onwards follows exactly as per the force coefficient method to obtain the final, interpolated coefficient value for pitch or yaw.

In the event that the instantaneous angles of attack and sideslip exceed that of what is available within the database, linear extrapolation will be implemented. Within small angles of attack, it can be adequately estimated that increases in the coefficient values are linearly proportional with increases in the angle of attack. For angles larger than that simulated, Equation (23) can be used to generate a coefficient derivative database for any given Mach number datapoint. This allows for the application of Equation (24) in the same manner to determine the coefficient derivatives between the largest two angle data points. This can then be used to extrapolate the instantaneous coefficient value with the following equation:

$$C_{x_{ij}} = C_{x_{j_{max}}} + \frac{dC_x}{d\alpha} (\alpha_i - \alpha_{max}) \tag{28}$$

where the max subscript refers to the maximum coefficient or angle of attack within the given coefficient database. It must be noted that linear extrapolation is not possible with Mach numbers exceeding that of what has been determined using CFD modelling as there is no clear linear relationship between the coefficient values.

#### 2.4. Parachute Model

The parachute deployment and recovery stages are an important part of the trajectory of the rocket (Figure 5). Once the parachute has been deployed, the characteristics of the parachute itself dominate the dynamics of the trajectory. The adopted modelling technique

is a modified version of the work presented in [39], which results in values within an acceptable engineering tolerance. That work used a simplified 3DoF method to model the rocket after the deployment of the parachute; however, the approach used in this article incorporates the generated additional drag into the already existing 6DoF model. A modified version of this method is present, with the notable change being that the force is applied in the wind direction rather than along the body axis. This allows for simpler integration into the existing 6DoF model while conserving the total amount of drag generated. The aerodynamic force on the point mass is dominated by the drag of the parachute. The drag is given by:

$$F_P = \frac{1}{2} \rho_{alt} V^2(t) C_D S(t) \tag{29}$$

where both the velocity and drag area ( $C_D S(t)$ ) are functions of time. The inflation model of the parachute is from Macha [46] and is shown below:

$$C_D S(t) = (C_D S)_0 \cdot \left( \frac{t}{t_f} \right)^\beta \tag{30}$$

$\beta = 1$  for slotted canopy parachutes

$\beta = 6$  for solid canopy parachutes

where  $t_f$  is the filling time and is calculated from the equation below, where  $n$  is the filling time index from [47].

$$t_f = \frac{n \cdot D_0}{V_0} \tag{31}$$

Finally, the parachute sizing is determined using the required touchdown velocity and the drag of the chosen parachute.

$$S_0 = \frac{mg}{q_{terminal} C_{D0}} \tag{32}$$

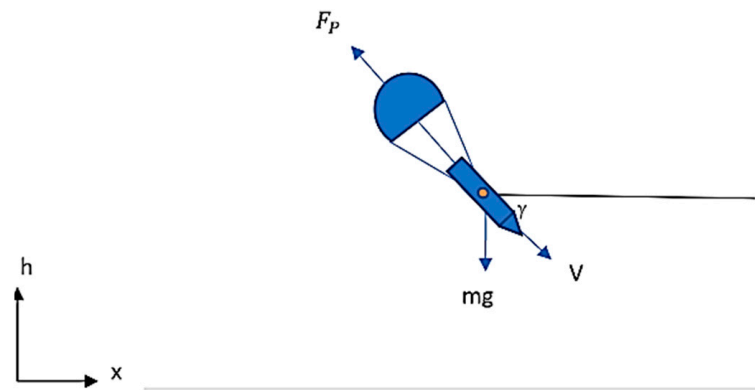


**Figure 5.** Diagram of parachute model dynamics.

This allows us to accurately model the drag caused by the parachute and the trajectory of the descending object. The specific type of parachute used in the trajectory simulation must be chosen. A summary of parachutes and their characteristics is presented in Table 2.

The trigger for the deployment of the parachute is the rocket reaching apogee. This is generally the point of deployment for a drogue parachute, and this method can be applied to trigger the deployment of the recovery phase at any arbitrary point chosen by the designer.

**Table 2.** Parachute models and characteristics [36].

Type	Constructed Shape $D_C/D_0$	Inflated Shape $D_P/D_0$	$C_{D,0}$	Average Angle of Oscillation	General Applications
Flat circular ribbon	1.0	0.67	0.45–0.50	0–3	Pilot, drogue, deceleration, descent
Conical ribbon	0.95–0.97	0.70	0.5–0.55	0–3	Pilot, drogue, deceleration, descent
Hemisflo ribbon	0.62	0.62	0.30–0.46	2	Supersonic drogue
Ringslot	1.0	0.67–0.70	0.56–0.65	5	Extraction, deceleration, descent
Disk-gap-band	0.73	0.65	0.52–0.58	10–15	Supersonic drogue, descent
Ballute	0.51	0.51	0.51–1.20	<1	Stabilisation, supersonic drogue

2.5. Thrust Model

The method for applying thrust to the rocket is simply by applying the force along the body axis of the rocket. This is a simple method but is representative of the force application in a real rocket. The thrust profile is able to be modelled in a way that is defined by the user, such as by creating a linear thrust model or using a dataset of the thrust developed in a commercial off-the-shelf rocket. These datasets are widely available and allow for the selection of an appropriate motor for the mission profile of the rocket.

2.6. Aeroelastic Model

The aerostructural response of the rocket governs the change in aerodynamic response due to structural loading. This is achieved using three steps:

1. Extraction of mode frequencies and mode shapes of CSD representation;
2. Mapping of aerodynamic pressures onto the CSD nodes;
3. Calculation of the aerodynamic response of the deformed shape.

This process is outlined in Figure 6 and closely follows the method outlined by [26].

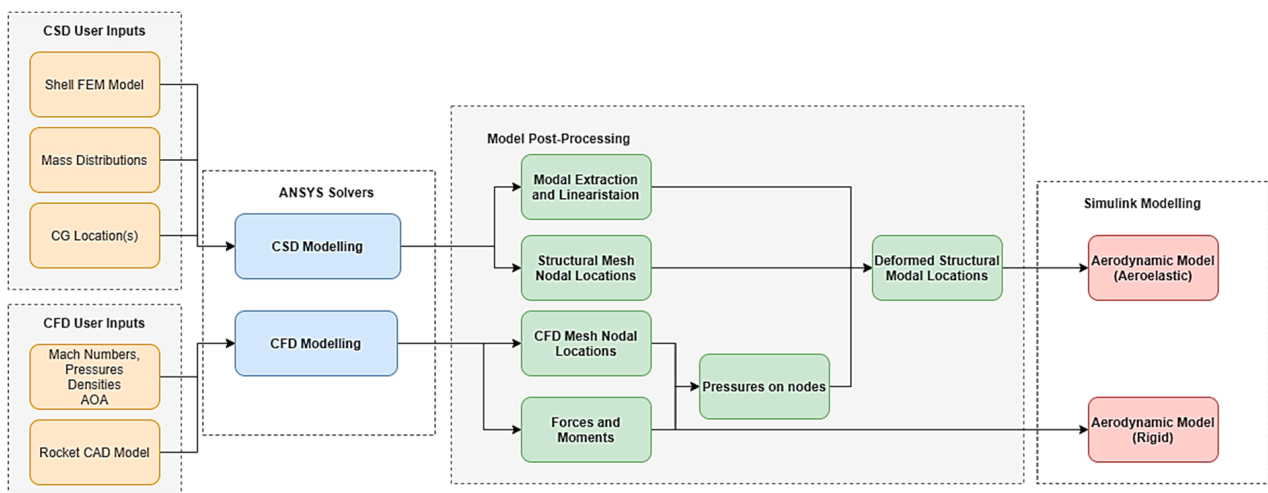


**Figure 6.** Overview of the methodology for the determination of aeroelastic properties.

The interplay between the CSD and the CFD modelling lies in the mapping of the pressures on the CFD mesh onto the structural mesh to determine the loads. This deformed shape is found using the superposition of the displacements due to the excitation of the CFD forces on the CSD mesh. This is outlined in Figure 7. The initial step in this procedure is to calculate the modal response of the rocket. A modal approach to finding the displacements of nodes in a system is useful as it greatly reduces the degrees of freedom, as the displacement is assumed to be a superposition of the basis functions. The general dynamic equation of motion for a system is given as:

$$M\ddot{q}(t) + C\dot{q}(t) + Kq(t) = F(t) \tag{33}$$

where  $M$  is the mass matrix,  $C$  is the damping matrix,  $K$  is the stiffness matrix,  $F$  is the force vector and  $q$  is the nodal displacement vector. In order for the displacement to be approximated as a superposition, the eigenmodes of the structure are chosen as the basis functions. These are found by a modal analysis of the undamped structure and satisfy the condition:

$$-\omega^2 MNx(t) + KNx(t) = 0 \tag{34}$$

where  $\omega$  is a diagonal matrix of the natural frequencies and  $N$  is the matrix of mass-normalised eigenmodes. We can then rewrite Equation (33) as:

$$MN\ddot{x}(t) + KN\dot{x}(t) = F(t) \tag{35}$$

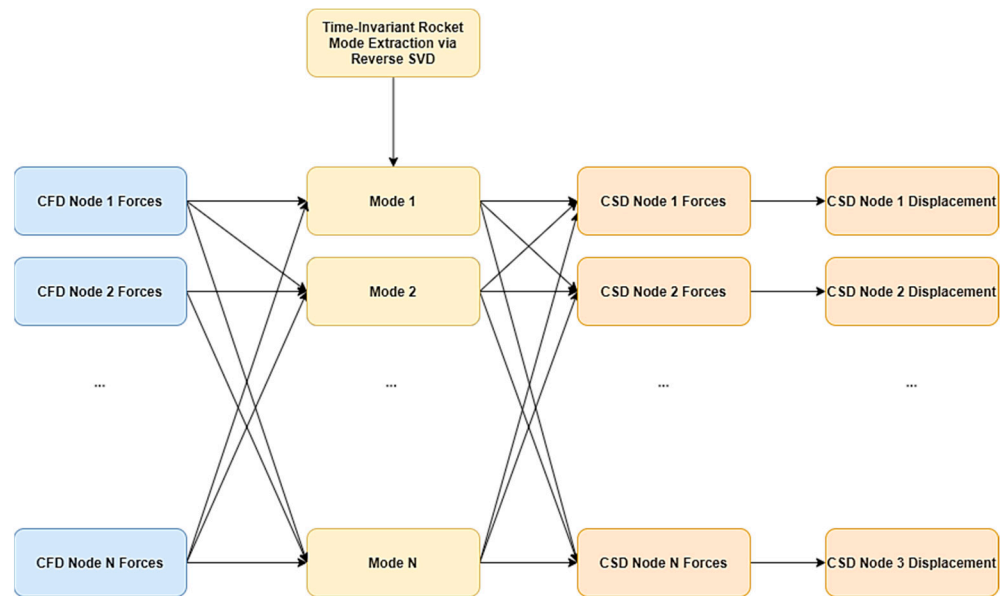


Figure 7. Overview of the MPR method.

This gives the ability to sum the modal displacements to find the approximate response of the system using the lower frequency modes from mode 1 to mode  $H$ .

$$q(t) \approx \sum_{i=1}^H N_i x_i(t) \tag{36}$$

Using this principal, we can multiply Equation (36) by  $N^T$  to find the modal equation of motion.

$$N^T MN\ddot{x}(t) + N^T BN\dot{x}(t) + N^T KNx(t) = N^T F(t) \tag{37}$$

For simplicity, we can denote these matrices as:

$$\begin{aligned} \bar{M} &= N^T MN \\ \bar{K} &= N^T KN \\ \bar{B} &= 2Z\sqrt{\bar{K}\bar{M}} \end{aligned} \tag{38}$$

where  $Z$  is the proportionate structural damping of each mode. Hence, we can reproduce Equation (37) as:

$$\bar{M}_{HH}\ddot{x}_H(t) + \bar{B}_{HH}\dot{x}_H(t) + \bar{K}_{HH}x_H(t) = F_H(t) \tag{39}$$

To improve the accuracy of the structural response over the course of the flight of the rocket, we can model the effects on the change in mass and centre of gravity of the system due to fuel burn in the motor. As the system eigenmodes are only valid for the point in time where  $\bar{M}_{HH}$  is valid, the derivation of a set of modes  $H^*$  that are valid at any arbitrary instant must be made.

This results in the equation below, which captures the free vibration of the system at a point in time where the mass is a function of time.

$$\bar{M}_{H^*H^*}(t)\ddot{x}_{H^*}(t) + \bar{B}_{H^*H^*}\dot{x}_{H^*}(t) + \bar{K}_{H^*H^*}x_{H^*}(t) = 0 \tag{40}$$

The change in the natural frequency with fuel burn is calculated by performing a modal analysis at different fuel burn times. As the mass and centre of mass of the rocket would change value and location, respectively, so would its frequency response.

Thus, across the rocket’s fuel burn, the  $i^{\text{th}}$  eigenmodes can then be combined to form a discrete value by:

$$N_{ik} = [N_i^0, N_i^1, \dots, N_i^k] \tag{41}$$

The singular value decomposition (SVD) is then given:

$$N_{ik} = U \cdot \Sigma \cdot V^T \tag{42}$$

Using the set of basis functions  $H^*$ , we can find the time-varying system matrices

$$\bar{M}(t) = N_{AH^*}^T M(t) N_{AH^*} \bar{K} = N_{AH^*}^T K N_{AH^*} \tag{43}$$

where the stiffness is assumed to be time-invariant. Then, we can reproduce Equation (34) in its time-varying form:

$$[-\omega^{k^2} \bar{M}^k V^k + \bar{K} V^k] \cdot \zeta(t) = 0 \tag{44}$$

where  $\omega$  is the matrix of instantaneous frequencies. By using the below equation, we can find the normal mode shape at each point in time throughout the course of the fuel burn.

$$N_{AH}^k = N_{AH^*} \cdot V^k \tag{45}$$

### 2.7. Mapping Aerodynamic Forces onto CSD Nodes

The MPR method maps the pressures on the cell faces onto the CSD nodes. The key requirement of this part of the methodology is to ensure that all CFD forces are conserved when they are applied to the CSD nodes. This is achieved by first finding the load at a fluid element centroid in the X, Y and Z directions by multiplying the pressure at the element centre by the area of the element in that direction. This gives:

$$[F_f] = \begin{matrix} R_x \\ R_y \\ R_z \end{matrix} = P_i \begin{bmatrix} A_x \\ A_y \\ A_z \end{bmatrix} \tag{46}$$

These forces and the moments applied to an element are equivalent to the force applied to the structural grid multiplied by the force equilibrium matrix found using CSD of a structural representation. This gives us:

$$F_{f,j} = S_{i,j} F_{s,i} \tag{47}$$

where  $F_f$  is the force on a fluid mesh element, and  $F_s$  is the force on a structural mesh node.

Using a nearest neighbour, we search around each fluid element centre  $i$  with an X, Y and Z coordinate represented by  $L_{f,i}$  for a set of neighbouring points on the structural grid represented by  $L_{s,i}$ . This allows us to increase the equilibrium matrix  $S_{i,j}$  to include all the neighbouring grid points  $N_i$ . We can therefore rewrite Equation (47) above as:

$$F_{f,j} = S_j F_s^j \tag{48}$$

This equation is used to apply an arbitrary load on the CSD grid onto the CFD grid, but it can be transformed to find a method of applying the fluid forces back onto the structural grid. This equation is given below.

$$F_s^j = [S_j]^T \left[ [S_j] [S_j]^T \right]^{-1} F_f^j \tag{49}$$

We can simplify this by rewriting it with a transformation matrix  $T$  where:

$$T_j = [S_j]^T \left[ [S_j] [S_j]^T \right]^{-1} \tag{50}$$

This gives:

$$F_s^j = T_j F_f^j \tag{51}$$

Using these two equations, we are now able to transform the forces from the fluid mesh onto the structural mesh, and back again. This allows us to calculate the deformation of the structure under the fluid loading and then transform this displacement from the structural mesh onto the fluid mesh.

### 2.8. Calculation of Aeroelastic Effects on the Trajectory

The final step in the MPR method is recalculating the forces and moments of the deformed shape. In order to calculate the effects of aeroelastic deformation on the lift and drag of the rocket, the deformation of the rocket will be calculated under the conditions (Mach, angle-of-attack, sideslip) found using the rigid body trajectory simulation. These values can then be used to calculate the deformed shape and the aerodynamic coefficients of the deformed rocket, which will then be fed back into the trajectory to create a 1-way fluid–structural interaction.

### 2.9. Model Verification Methods

The models and methods outlined thus far do not account for small errors in either engineering tolerances in the physical rocket or in the collection of the CSD and CFD data. Hence, it is necessary to provide a range of probabilistic outcomes that take these errors into account in order to have confidence in the outputs of the simulation.

As discussed in the Introduction Section, the MCS method will be adopted to generate probabilistic results from nominally deterministic functions [13]. The method of application for each is produced below using the methods proposed by Eerland [42]. This method applies small uncertainties to the force coefficients using multiplication and to the initial launch angles using addition (Table 3).

**Table 3.** Monte Carlo probability distributions application methods.

Variable	Application Method
Drag coefficient	Multiplication
Centre of pressure	Multiplication
Normal coefficient	Multiplication
Parachute drag coefficient	Multiplication
Thrust curve	Multiplication
Declination launch angle	Addition
Azimuth angle	Addition

**Aerodynamic coefficient distributions:** the distribution used for the aerodynamic coefficients uses a simplified method for calculating the approximate error distribution. These results are found by comparing the deviation of the converged outputs of the CFD analyses. Using this comparison, we are able to find a value for the lift and drag coefficients

that reflects the uncertainty of the results of the CFD analysis, solved using the equations presented in previous sections.

**Centre of Gravity displacement distribution:** the uncertainty in the location of the centre of gravity is also considered as part of the MCS. The distribution of the centre of gravity positions interacts with the distribution of the centre of pressure thereby affecting the moment coefficient of the rocket and thus has a major effect on the dynamics of the rocket. Reasons for the uncertainty in the location of the centre of gravity may include manufacturing tolerances and uncertainty in the fuel burn of the motor.

**Thrust distribution:** As the thrust is given by a commercial off-the-shelf motor, the distribution is assumed to ensure the rocket meets the USA Rocket Motor Certification.

**Launch angle distribution:** the launch angles are applied using addition as it is assumed that the error in the angle is independent of the magnitude of the launch angle. That is, a launch angle of 45° will have the same error as a launch angle of 70° or 80°. This is the method used by [41] who found that an assumed standard deviation of 1° in the pitch and yaw provides accurate results.

### 3. Application Case Study

This section presents a case study performed to verify the proposed method for high-fidelity trajectory simulation. The sounding rocket utilised in this case study is the *Ad Astra II* rocket (Figure 8).

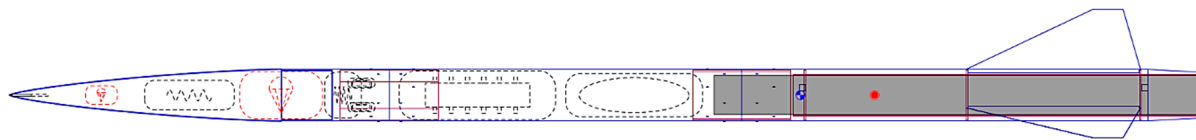


Figure 8. Ad Astra II rocket [48].

The model consists of three main airframe components: a nosecone, body tube, three fins and a boattail. The internal structure of the rocket additionally includes a motor mount tube and centring rings. These are presented within Table 4.

Table 4. Rocket Dimensions.

Total length (m)	2.941
• Nose length (m)	0.695
• Body tube length (m)	2.115
• Boattail length (m)	0.131
Diameter (m)	0.131
Airframe thickness (m)	0.00191
Centring ring thickness (m)	0.00467
Fin thickness (m)	0.0051
Exposed fin root chord (m)	0.445
Reference fin root chord (m)	0.6044
Fin tip chord (m)	0.075
Exposed fin surface area (m <sup>2</sup> )	0.152
Reference fin surface area (m <sup>2</sup> )	0.0739

#### 3.1. Aerodynamic Mesh Convergence Analysis

To ensure that the mesh used was sufficient to capture the dynamics of the fluid around the body, a mesh convergence study was conducted. The aim of this study is to find the least number of mesh elements that accurately resolves the flow field so that the

speed of calculations is increased. For this study, three mesh sizes were tested at a Mach number of 2.2, an angle of attack of 2.4 degrees and at sea level. The results of this study are presented below.

From the results in Table 5, we can see that there is little difference between the three meshes, with only a 3.6% difference in the drag coefficient between the coarsest and the finest meshes. We also notice that the medium mesh captures the flow field almost exactly as well as the fine mesh. Hence, we select a mesh size of 370 k elements for the analysis. Figure 9 shows a cross-section of the FLUENT mesh. The notable features are the fineness of the mesh close to the surface of the rocket body, in particular at the tip of the nosecone. Figure 10, on the other hand, presents a close-up cross-section of the mesh at the nosecone. Here, we can also see the 15 inflation layers on the surface of the rocket that capture the flow conditions close to the wall.

**Table 5.** Mesh sensitivity study.

Mesh	Number of Elements	Lift Coefficient	Drag Coefficient
Fine	430 k	1.066	0.57
Medium	370 k	1.066	0.571
Coarse	248 k	1.02	0.55

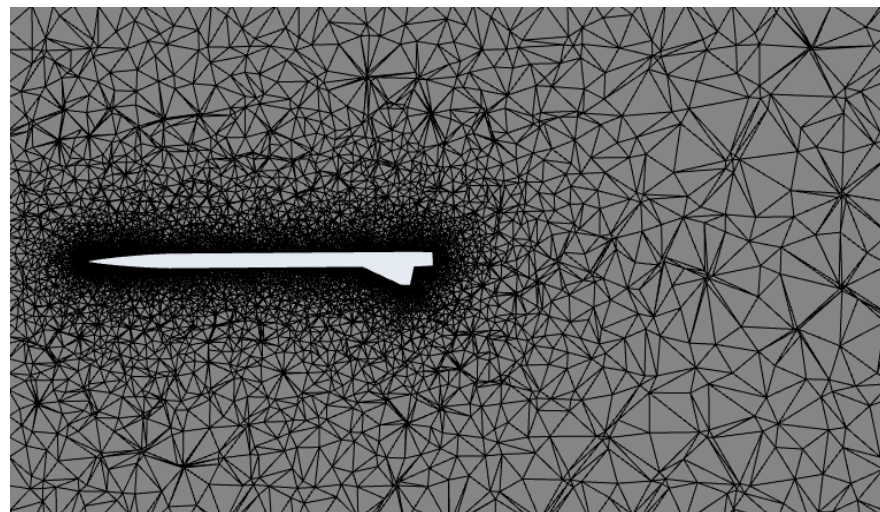


**Figure 9.** Cross-section of FLUENT mesh.

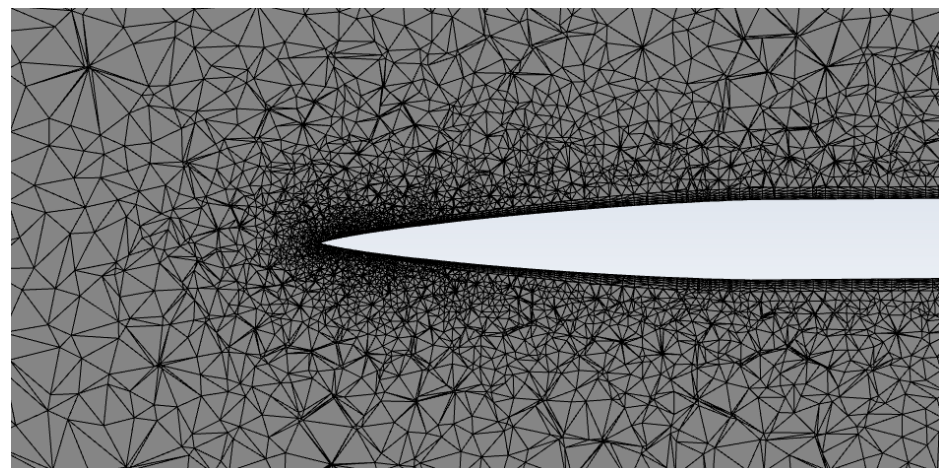


**Figure 10.** FLUENT mesh at nosecone.

### 3.2. Change in Moment Coefficient due to CG Displacement

The moment about the centre of gravity as the latter’s location moves towards the nose due to fuel burn is depicted in Figure 11. This graph shows the change in the moment coefficient as the centre of gravity moves from 2.0965 m from the nose to 1.9288 m from the nose.

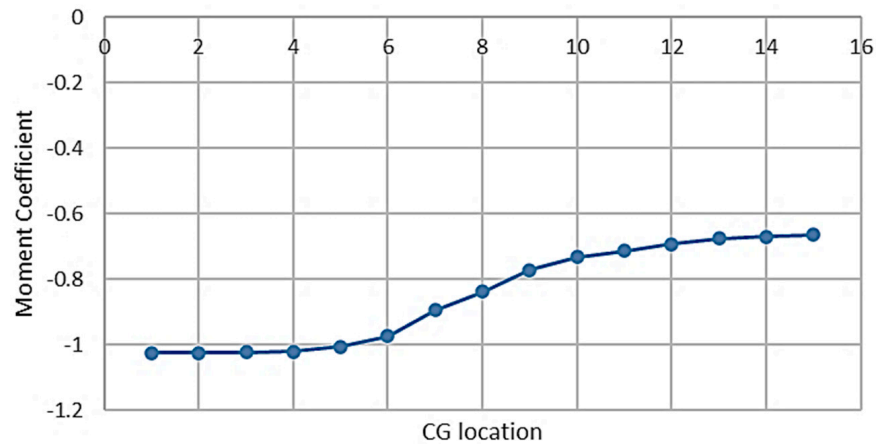


Figure 11. CG location vs moment coefficient.

### 3.3. Aerodynamic Coefficient Analysis

To determine the aerodynamic derivatives, a database of aerodynamic coefficients must be created that covers the entirety of the flight envelope. Based on preliminary trajectory simulations, the CFD analyses were performed at Mach numbers of 0.3, 0.5, 0.7, 0.8, 0.85, 0.9, 0.95, 1.0, 1.05, 1.1, 1.15, 1.2, 1.5, 1.5, 2.2 and 2.6. These Mach numbers were tested at angles of attack of 0 degrees, 1.2 degrees and 2.4 degrees, and at a sideslip angle of 2 degrees. The concentration of cases in the transonic region was deliberately chosen as the transonic region is the most nonlinear region. Figures 12 and 13 display the lift and drag coefficients for the angle of attack of 2.4 degrees.

We can see that the resolution of the test cases is able to accurately capture the Mach effects on the lift and drag coefficients. Visually, we can identify the presence of shockwaves by plotting the contours of the Mach number on a plane that gives a cross-section of the rocket (Figure 14).

The lift, drag and moment coefficients generated across the different Mach numbers, angle of attack and sideslip angles are plotted in Figures 15–20. These plots visualise the datasets applicable within the trajectory simulation of the model for each major coefficient as a function of incidence angle and Mach number and outline the bounds where interpolation is possible.

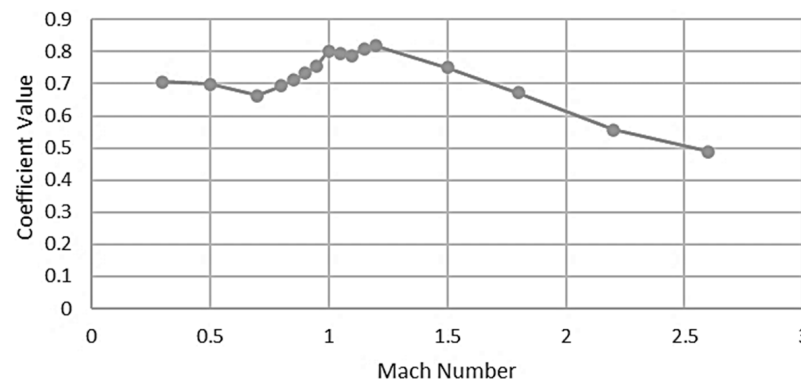


Figure 12. Mach number vs lift coefficient for an angle of attack of 2.4 degrees.

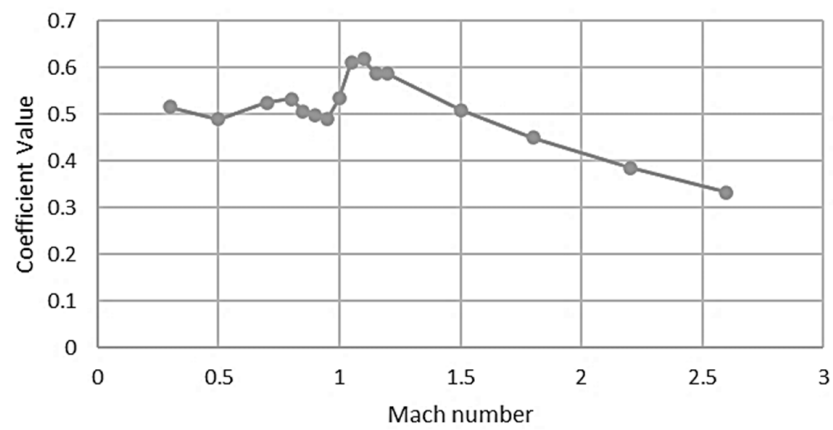


Figure 13. Mach number vs drag coefficient for an angle of attack of 2.4 degrees.

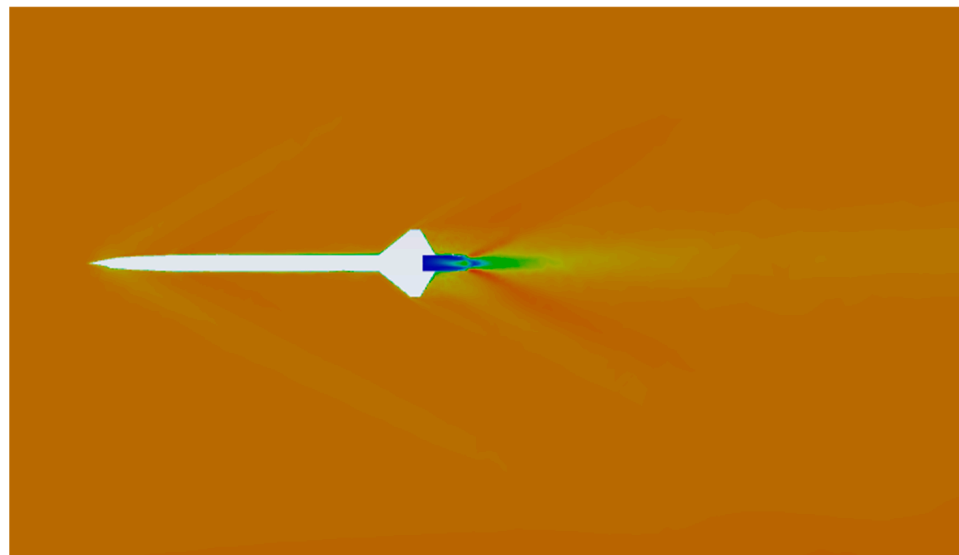


Figure 14. Contours of the Mach number at 2.4-degree AoA and 2.2 Mach.

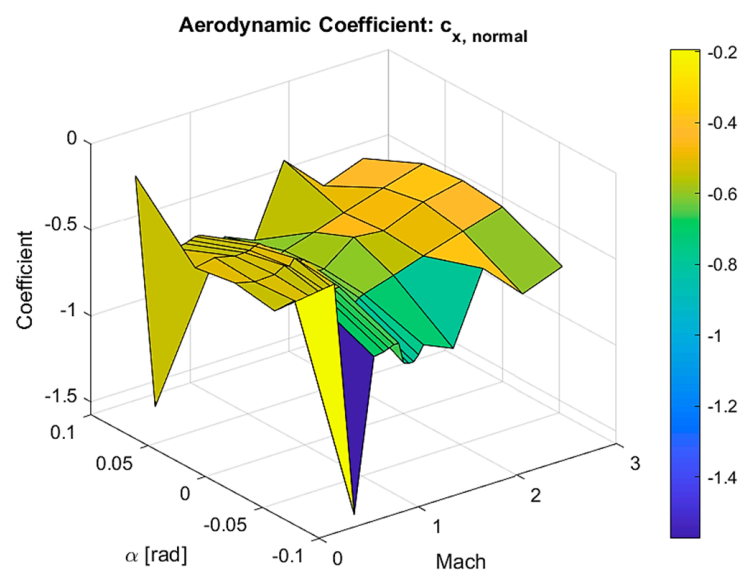


Figure 15. Axial drag coefficient as derived from the angle of attack and Mach number.

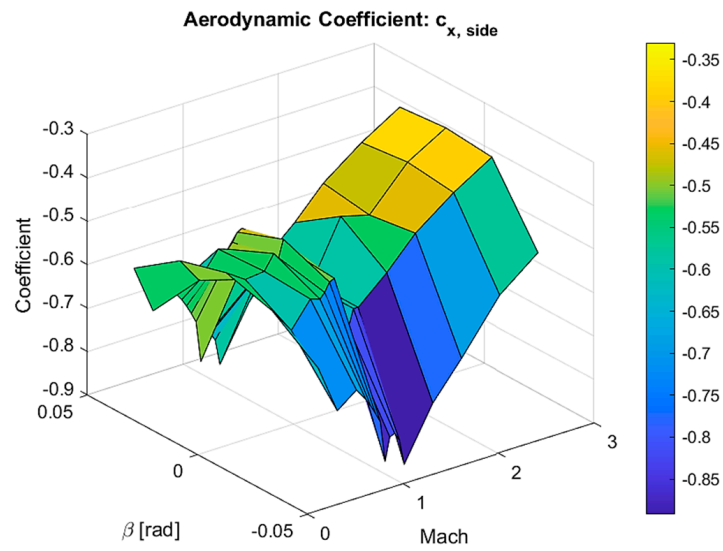


Figure 16. Axial drag coefficient as derived from the sideslip angle and Mach number.

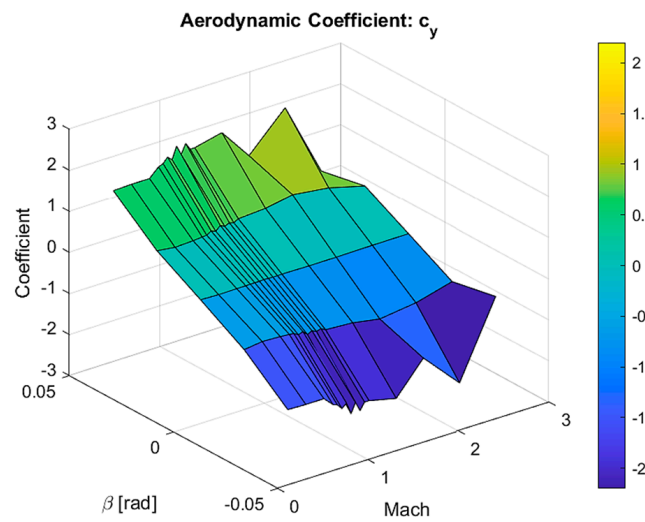


Figure 17. Side force coefficient as derived from the sideslip angle and Mach number.

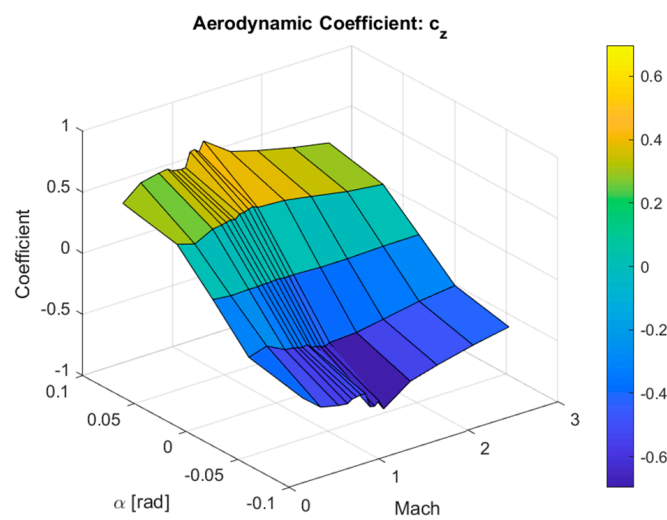


Figure 18. Normal force coefficient as derived from the angle of attack and Mach number.

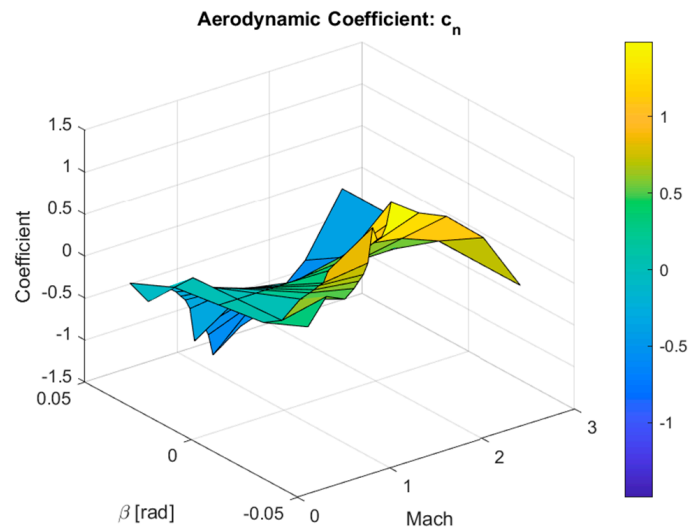


Figure 19. Yaw (forcing) moment coefficient as derived from the sideslip angle and Mach number.

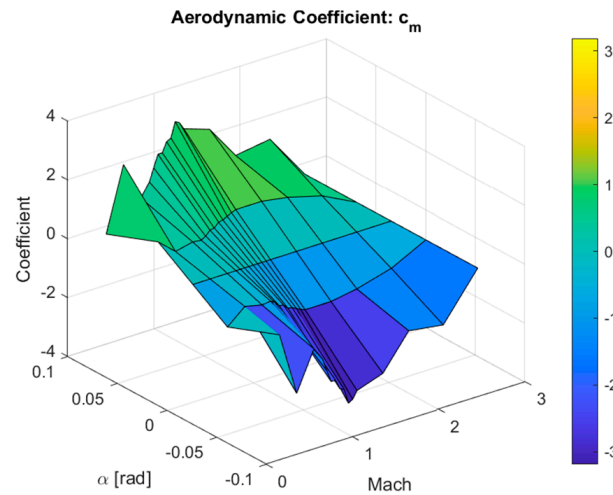


Figure 20. Pitch (forcing) moment coefficient as derived from the angle of attack and Mach number.

### 3.4. Parachute Model

Using the design criteria and the mission profile, a disk-gap-band parachute was selected for use in this rocket. This is due to the fact that it can act as a supersonic drogue chute and also as a main chute. The drag coefficient was assumed to be equal to 0.55, as this is the midpoint of the range of 0.52–0.58 given by Maydew [36]. As this is a slotted parachute, the value of  $\beta$  in Equation (30) is equal to 1, which results in a linear inflation function.

### 3.5. Thrust Model

The propulsion method used within this case study is the Commercially off-the-Shelf (CotS) Cesaroni O3400 “Imax” solid fuel motor. Its thrust curve can be seen in Figure 21 with data sourced from [49]. Complete information regarding the specific properties of motor grain geometry was not available; however, the boost duration and burn profile suggest a progressive burning internal star configuration [50]. These factors will be elaborated on within the following sections for their effects on the mass of the rocket in determining its aeroelastic behaviour.

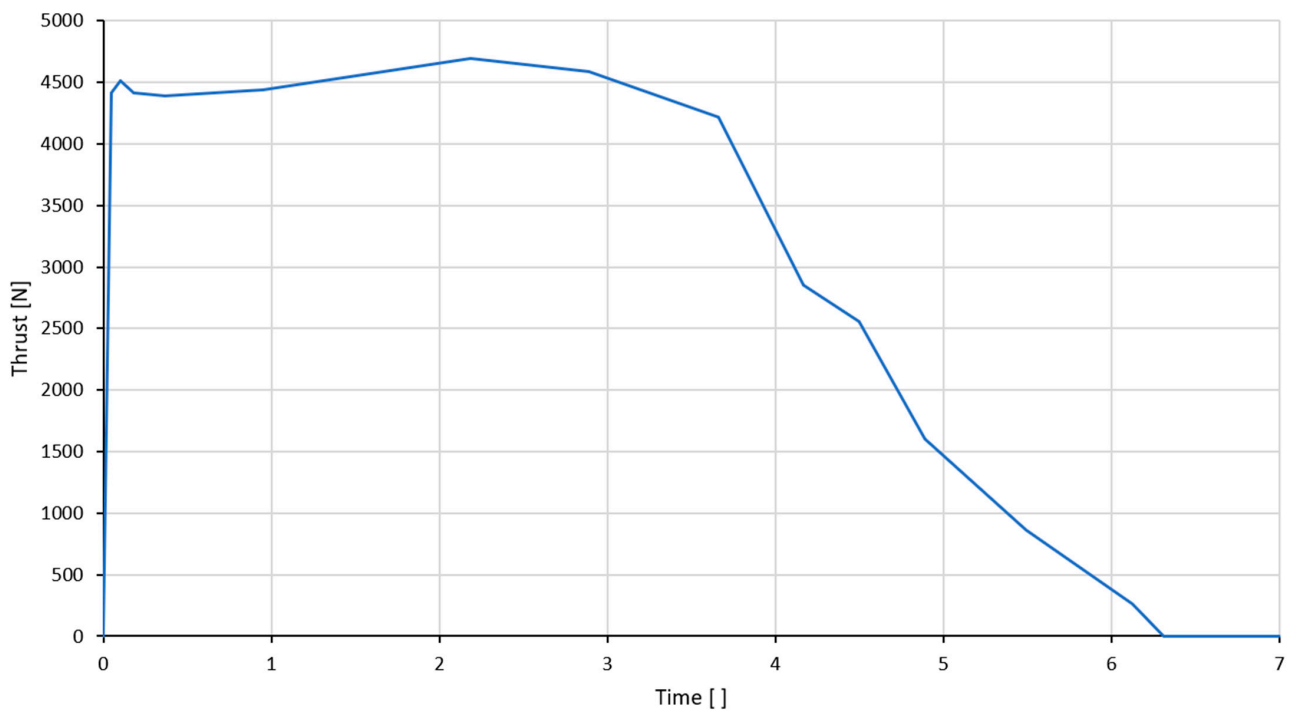


**Figure 21.** Cesaroni O3400 “Imax” thrust curve.

### 3.6. Monte Carlo Distributions

The Monte Carlo distributions were found using the method outlined in previous sections. A summary of the resulting probabilities is given in Table 6.

**Table 6.** Monte Carlo Coefficient Distributions.

Variable	Probability Distribution	Application
Drag coefficient	$N(1, \sigma^2), \sigma = 0.004$	Multiplication
Lift coefficient	$N(1, \sigma^2), \sigma = 0.0315$	Multiplication
Centre of gravity	$N(1, \sigma^2), \sigma = 0.00612$	Multiplication
Parachute drag coefficient	$N(1, \sigma^2), \sigma = 0.1$	Multiplication
Thrust curve	$N(1, \sigma^2), \sigma = 0.0011$	Multiplication
Declination launch angle	$N(0, \sigma^2), \sigma = 1$	Addition
Azimuth angle	$N(0, \sigma^2), \sigma = 1$	Addition

### 3.7. Trajectory Simulation Results

The trajectory was obtained via implementation within the Simulink model. The results of this simulation are expressed as the translational and rotational position, velocity and acceleration in the Earth-Centred-Inertial, Earth-Centred-Earth-Fixed, north–east–down and body frames. We also express the angle of attack and slide slip angles. The outputs are shown in Figure 22. For this simulation, the launch angle is 85 degrees to the horizontal. Here, we present the results of a trajectory simulation performed without the parachute.

These results show that the rocket follows a roughly parabolic flight plan, as is to be expected for this type of rocket. It reaches a maximum velocity of 566 m/s, which is a Mach number of 1.66. This means that the Mach number remains inside the range of values found with the CFD analysis presented previously, which found the aerodynamic coefficients up to a Mach number of 2.6.

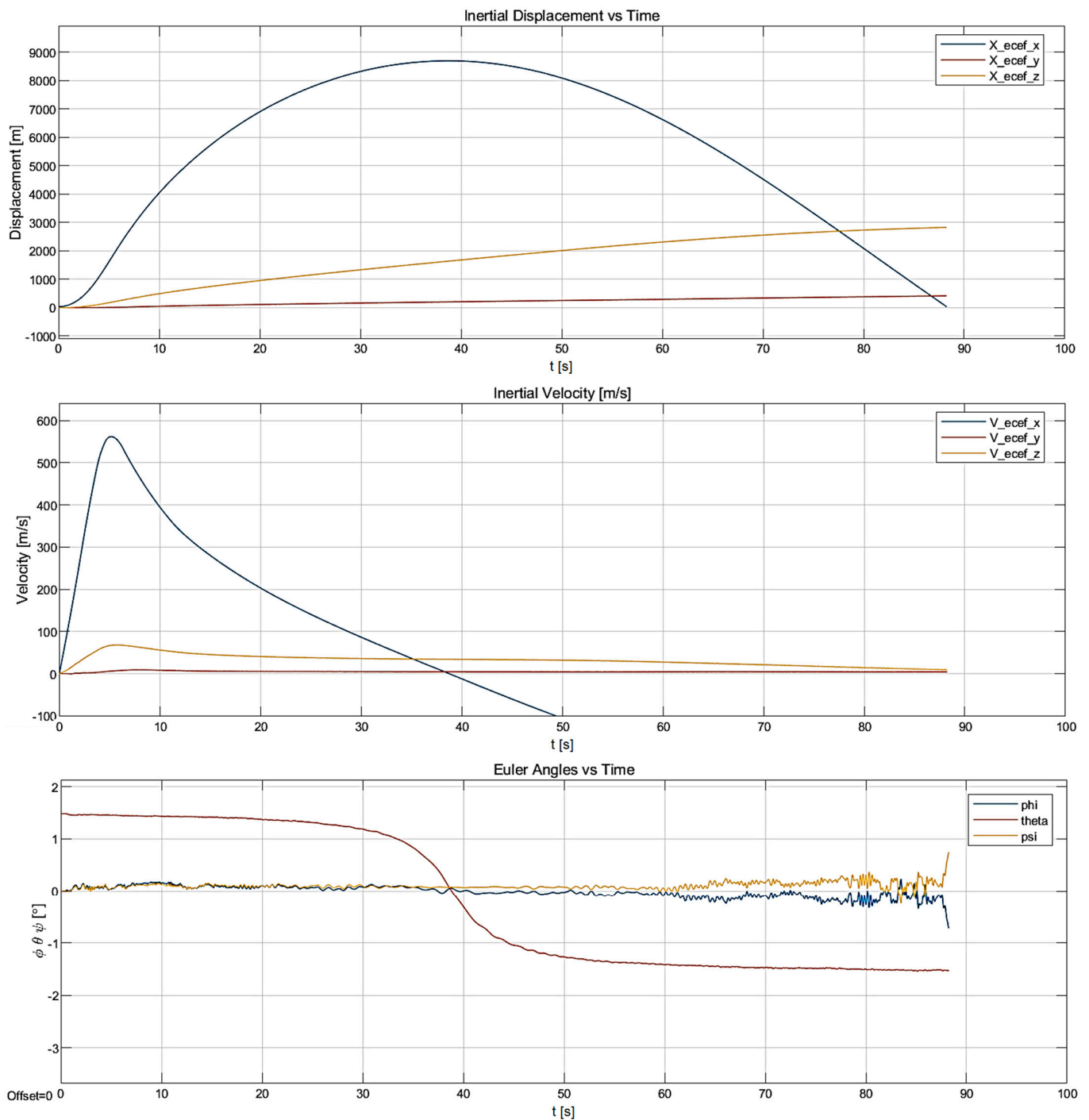


Figure 22. Inertial axis results.

Next, the results for the body axis are presented in Figure 23. Here, we see the effects of the turbulence modelling are apparent in the oscillations in the body’s angular rates and accelerations. The maximum angle of attack and sideslip angles were both 0.0625 radians, which is 3.6 degrees. This angle is outside the maximum value testing in the aerodynamic analysis; however, it is still not a high angle, so a linear extrapolation to this angle remains valid.

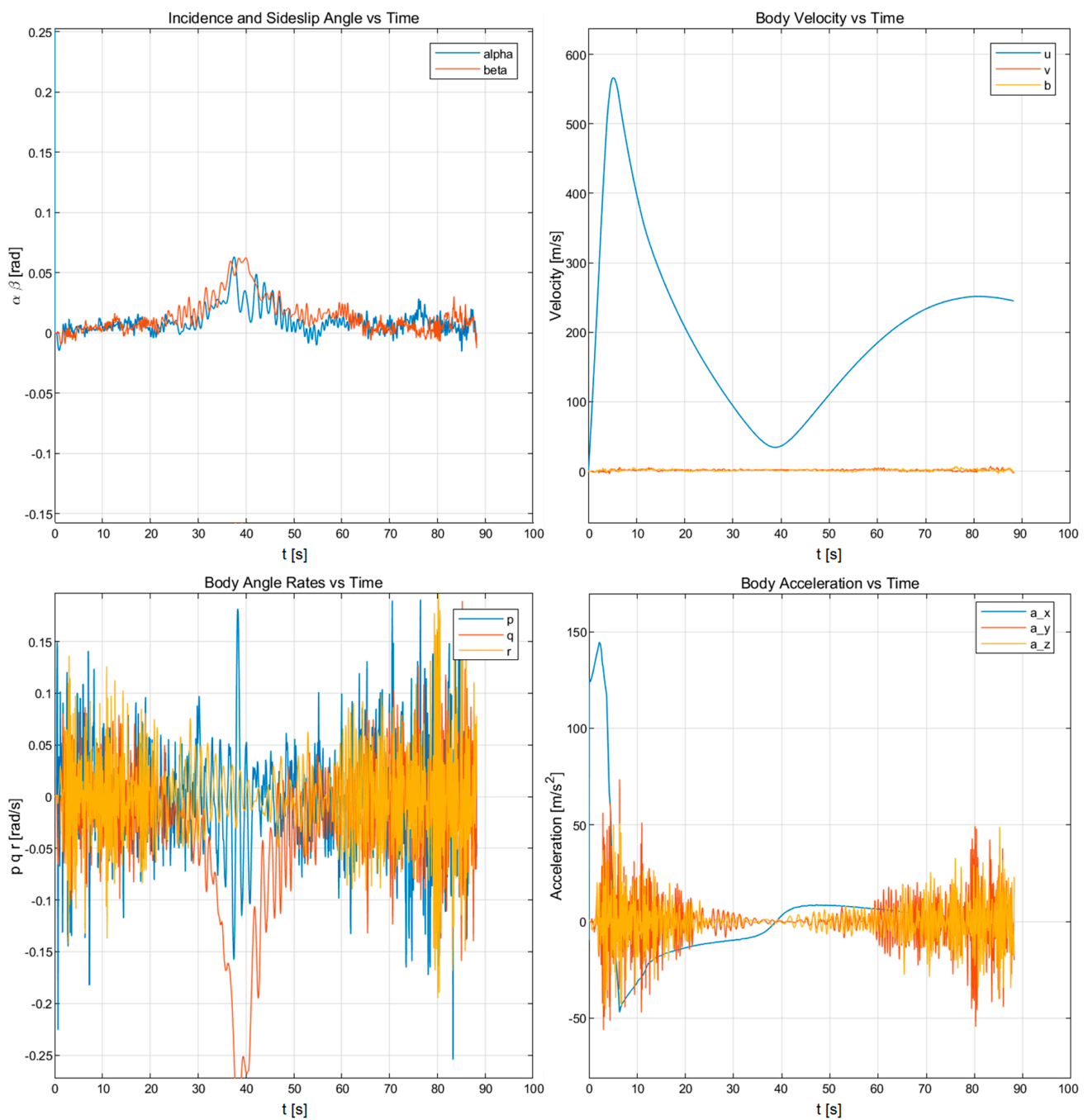


Figure 23. Body axis results.

### 3.8. Aeroelastic Analysis

The material of the rocket itself is made up of S-Glass composite and aluminium 6061-T6. The aluminium is utilised within the boattail of the rocket, and the rest of the structure is made of composites. The material properties are outlined in Table 7.

Table 7. Rocket Material Properties.

	S-Glass Composite [49]	Aluminium 6061-T6 [51]
Density ( $kgm^{-3}$ )	2480	2700
Young's Modulus (MPa)	85,500	68,900
Poisson's Ratio	0.22	0.33

While an appropriately structured solid element model would provide the highest level of fidelity for the model, the nature of the geometry and expected loading conditions allow for simplifications. The thickness of the airframe skin, centring rings and fins are constant throughout each part. Additionally, with these thicknesses being 1.91 mm, 4.67 mm and 5.1 mm, respectively, they are significantly less than the total length of the rocket. These aspects allow for their adequate representation as shell elements. The main benefit of this is to allow for significantly less computational intensity throughout FSI iterations while maintaining high accuracy with regards to a model using solid elements, as documented in [26]. General linear SHELL181 elements have been utilised for meshing the complete rocket structure. With the axisymmetric structure, quadrilateral elements were implemented throughout most of the model. The regions that differed were the nose cone, where the blunt tip typically resulted in many high aspect ratio elements. The solution was to maintain a quadrilateral dominated mesh, where triangular elements would be meshed toward the tip. Element sizing was controlled globally; however, with the smaller nature of the centring rings, their element sizing was controlled locally. The different surfaces within the model are connected with tie constraints to allow for the transfer of loads throughout the structure.

Beyond the structural elements, the rocket masses needed to be modelled as these would significantly affect the modal response. The components considered here are the drogue and main chutes, avionics bay and the scientific payload. Being non-structural, these will be represented as point masses located along the rocket’s centreline and constrained to appropriate surfaces with MPC Beam constraints. As these components have physical dimensions, the mass moment of inertia was additionally calculated as cylindrical prisms, which have also been implemented within the model. These are listed in Table 8. Table 8 and the component centroid location relative to the nose cone are provided in Table 9. The mass placements within the CSD model are shown in Figure 24. Regarding the solid fuel motor mass, as this varies throughout flight time, the changes in mass and inertia need to be correctly represented. In keeping with the star fuel grain geometry, the centroid of the rocket motor does not change over the course of flight. However, the change in fuel grain radius needs to be accounted for within the motor’s changing mass moment of inertia. As such, the motor is represented within the rocket as a hollow cylinder. Inertia calculations are detailed in Table 10, while the motor’s grain geometry characteristics are given in Table 11. The motor change in mass is represented in Figure 25.

Table 8. Component centroid location relative to the nose cone.

Component	Location (m)
Drogue Chute	0.235
Main Chute	0.694
Avionics	1.19
Payload	1.59
Motor	2.4275

Table 9. Component mass and mass moment of inertia values.

Component	Mass (kg)	Length (m)	Radius (m)	I <sub>x</sub> (kgm <sup>2</sup> )	I <sub>y</sub> (kgm <sup>2</sup> )	I <sub>z</sub> (kgm <sup>2</sup> )
Drogue Chute	0.045	0.08	0.0225	$1.13906 \times 10^{-5}$	$2.40029 \times 10^{-5}$	$2.40029 \times 10^{-5}$
Main Chute	0.879	0.21	0.12	0.0063288	0.003275892	0.003275892
Avionics	1.4	0.4	0.124	0.0107632	0.018749414	0.018749414
Payload	4.4	0.65	0.109	29.7025	176.0418431	176.0418431

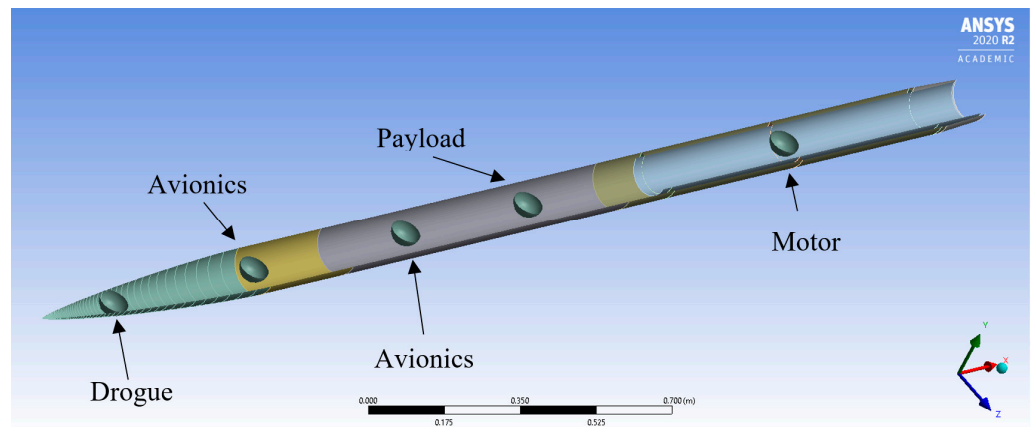


Figure 24. Annotated point mass locations within the rocket cross-section.

Table 10. Motor mass and mass moment of inertia values.

Index	Time (s)	Mass (kg)	Inner Fuel Grain Radius (m)	I <sub>x</sub> (kgm <sup>2</sup> )	I <sub>y</sub> (kgm <sup>2</sup> )	I <sub>z</sub> (kgm <sup>2</sup> )
0	0	11.2720	0.0176	0.0104	17.3526	17.3526
1	0.04	11.2296	0.0177	0.0104	17.2874	17.2874
2	0.052	11.2026	0.0178	0.0104	17.2459	17.2459
3	0.101	11.0852	0.0180	0.0103	17.0654	17.0654
4	0.19	10.8721	0.0180	0.0101	16.7373	16.7373
5	0.38	10.4237	0.0191	0.0099	16.0483	16.0483
6	0.965	9.0391	0.0215	0.0090	13.9193	13.9193
7	2.176	6.0734	0.0267	0.0068	9.3568	9.3568
8	3.658	4.3040	0.0298	0.0052	6.6331	6.6331
9	4.17	2.4829	0.0329	0.0033	3.8280	3.8280
10	4.493	1.5119	0.0346	0.0021	2.3314	2.3314
11	4.881	1.0435	0.0354	0.0015	1.6093	1.6093
12	5.483	0.6092	0.0362	0.0009	0.9396	0.9396
13	6.137	0.2080	0.0369	0.0003	0.3208	0.3208
14	6.322	0.0123	0.0372	0.0000	0.0190	0.0190

Table 11. Solid motor fuel grain geometry.

Motor Type	Star
Web Fraction	0.45
Outer Radius	0.0392125
Initial Inner Radius	0.0176456
Total Grain Length (6GXL)	1.238504

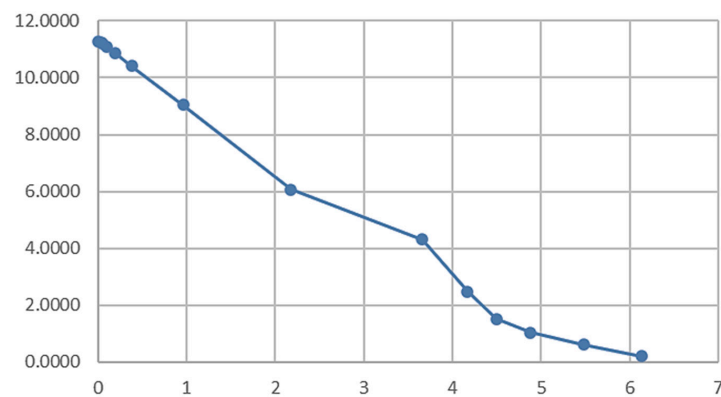


Figure 25. Motor mass over time.

### 3.8.1. Mesh Sensitivity Analysis

Similar to the CFD modelling, a mesh sensitivity study was undertaken to ensure the validity of the results. Three different mesh fidelities were used to determine the validity of the CSD modelling. This was controlled through the setting of the global mesh size. Specific mesh information for the mesh cases studied are elaborated within Table 12. The nominal result of the study can be referred to in Table 13, with Table 14 showing the results normalised to the coarsest mesh.

**Table 12.** Mesh information.

	Coarse	Medium	Fine
Element Size (mm)	30	14.82	10
Elements	2284	9833	20713
Average Aspect Ratio	1.378	1.2282	1.216
CP Time (s)	5	30	4686
Actual Time (s)	41	106	4823
Relative CP Time	1	2.585366	117.6341

**Table 13.** Nominal mesh sensitivity results (Fully Fuelled Rocket).

Real Modes (Hz)	Coarse	Medium	Fine
1	11.8330	11.952	12.913
2	14.5080	14.946	15.596
3	41.1250	41.452	41.917
4	43.3300	43.605	44.169
5	54.2420	55.274	56.549

**Table 14.** Normalised sensitivity values relative to coarse mesh (Fully Fuelled Rocket).

Mode (Hz)	Coarse	Medium	Fine
1	-	1.010	1.091
2	-	1.030	1.075
3	-	1.007	1.025
4	-	1.008	1.019
5	-	1.006	1.019
6	-	1.019	1.043
Average Difference	-	0.013	0.045

The results across the different mesh fidelities show similar values in the frequencies of the first five modes of the rocket. As modes 1 and 2 represent orthogonal shapes for the 1st-order bending mode and 3 and 4 are likewise for the 2nd-order bending modes, the frequencies for each are paired throughout all the studies conducted. The trend in pure radial mode response is also quite similar across the different resolutions. What can be seen, however, is that all cases are quite similar to each other, with the finest mesh only varying by 4.5% from the coarse mesh. The quality of the medium and finest mesh, however, is greatly increased over the coarse mesh, with the average aspect ratio being approximately 1.2, whereas the coarse mesh is 1.3. The marginal difference in quality between these two meshes, however, can be contrasted by the significantly longer runtime. The fine mesh requires 45.5 times the run time of the medium mesh for a marginally different result. With these differences considered, the modal analysis will use a modified medium mesh, wherein local refinement such as mesh biasing within the nose cone allows for the further elimination of high aspect ratio elements. Figure 26 visualises the final mesh used within the rocket.

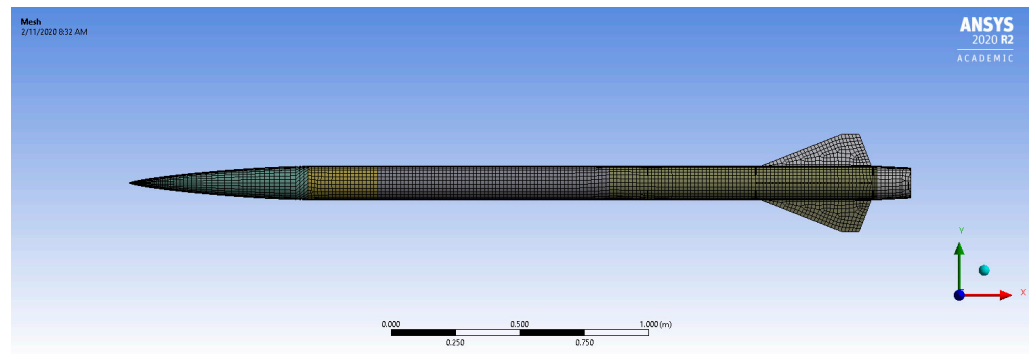


**Figure 26.** Rocket Mesh.

### 3.8.2. Modal Analysis

As the rocket is not externally constrained throughout the flight, the analysis was accomplished in absence of boundary conditions. This results in the first six exhibiting 0 Hz in frequency, representing the first six rigid body modes. This results in modes 7 and 8 being the 1st-order bending modes of the rocket X–Y and X–Z planes; modes 9 and 10 being the 2nd-order bending modes of the rocket; and mode 11 being the pure radial mode [52]. These first five real modes are of interest within this study and thus will be described as modes 1–5. Figures 27–31 visualised these modes. As the change in mass affects the visualisation of the mode shapes very little, only the first five modes are showcased here for the fully fuelled case.

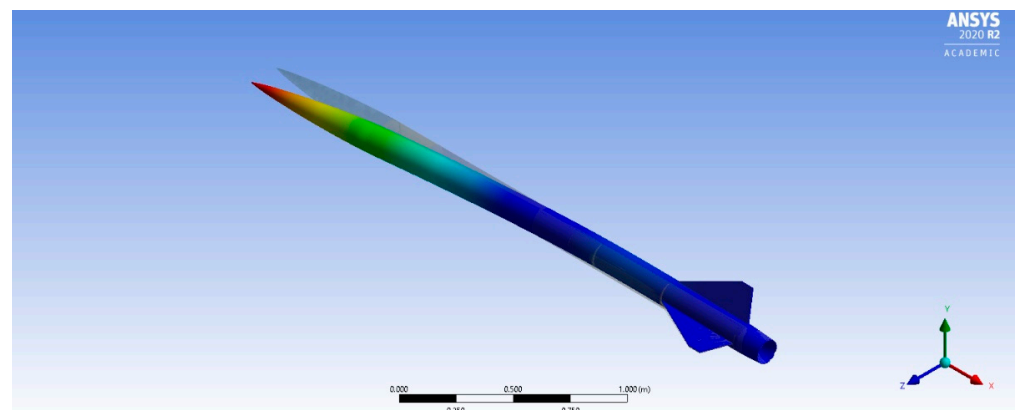


**Figure 27.** First-Order Bending Mode Shape (X–Z Plane).

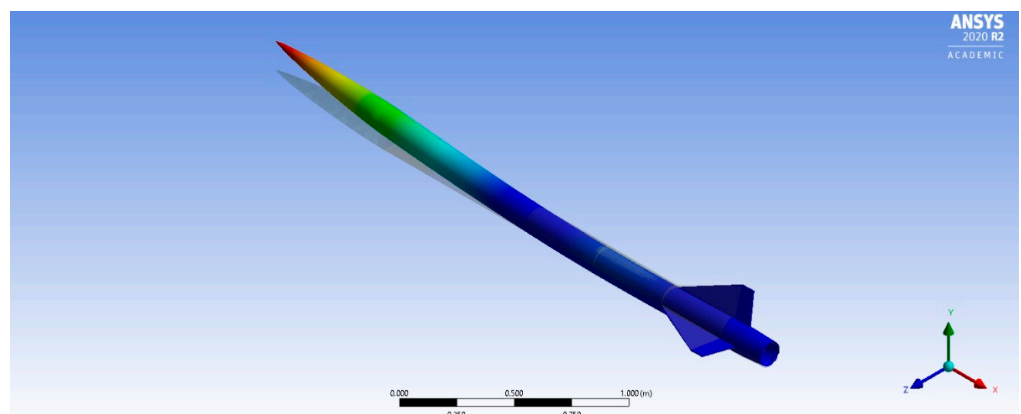


**Figure 28.** First-Order Bending Mode Shape (X–Y Plane).

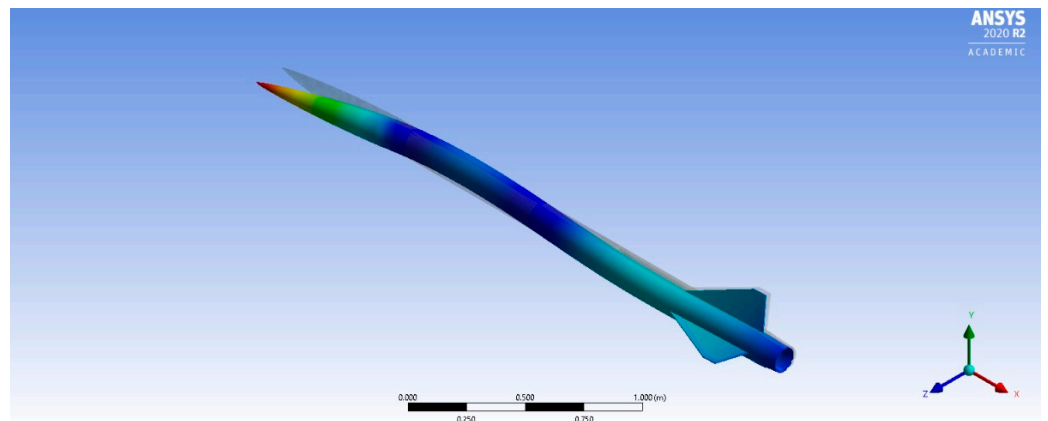


**Figure 29.** Second-Order Bending Mode Shape (X–Z Plane).

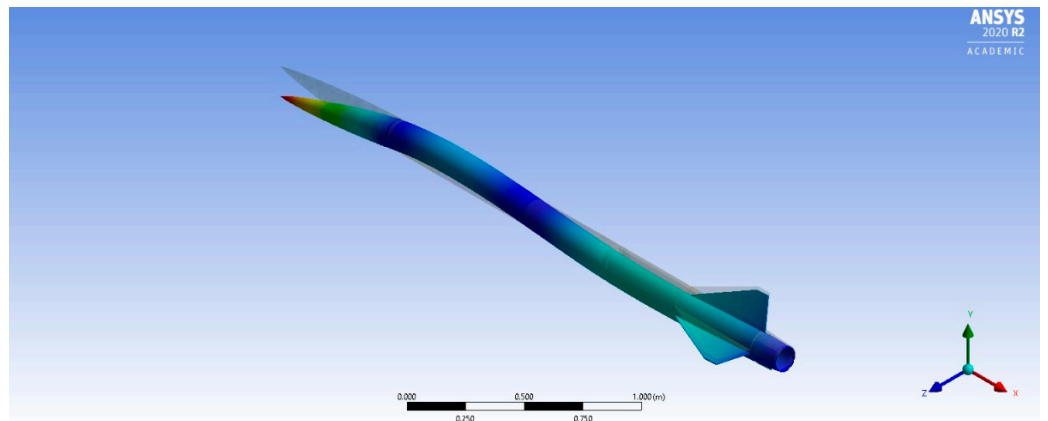


**Figure 30.** Second-Order Bending Mode Shape (X–Y Plane).

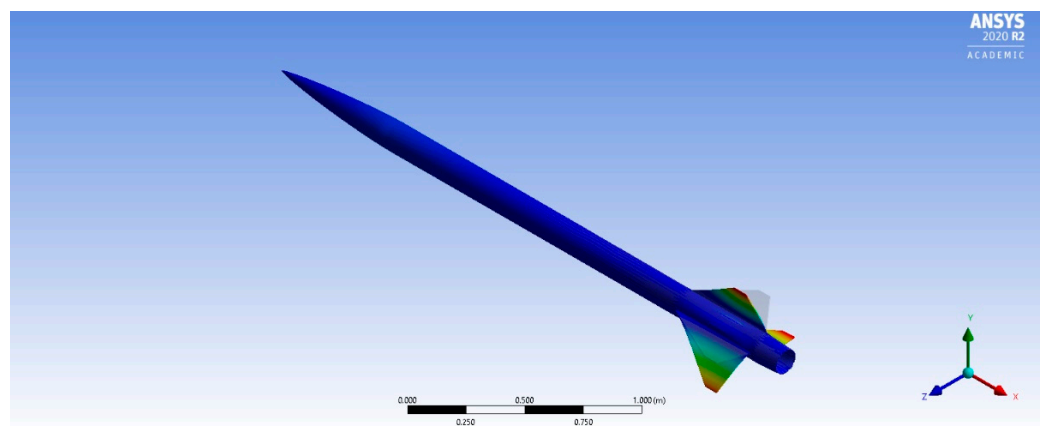


**Figure 31.** Pure Radial Mode Shape (X–Z Plane).

In consideration of the change in the motor mass throughout the flight, Figure 32 shows the change in the overall rocket mass over time and Figure 33 shows the time-frequency response of the rocket as the fuel is burnt.

It can be seen that with decreasing mass, the frequency response of the rocket shifts upwards. As the inertia of the rocket likewise decreases, the frequency further shifts, resulting in larger differences between the different modal frequencies toward the end of the fuel burn. The rocket moment inertia along the x-axis does not change significantly throughout the flight, and thus the 5th mode does not shift significantly over time. In short,

these results indicate a suitable representation of the rocket to be used within the aeroelastic modelling of the rocket.

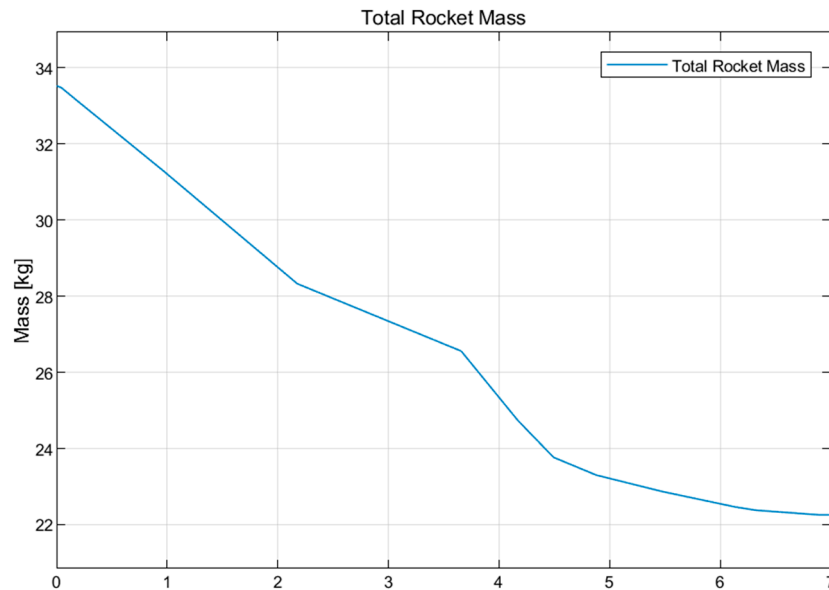


Figure 32. Total rocket mass over first 7 s of flight.

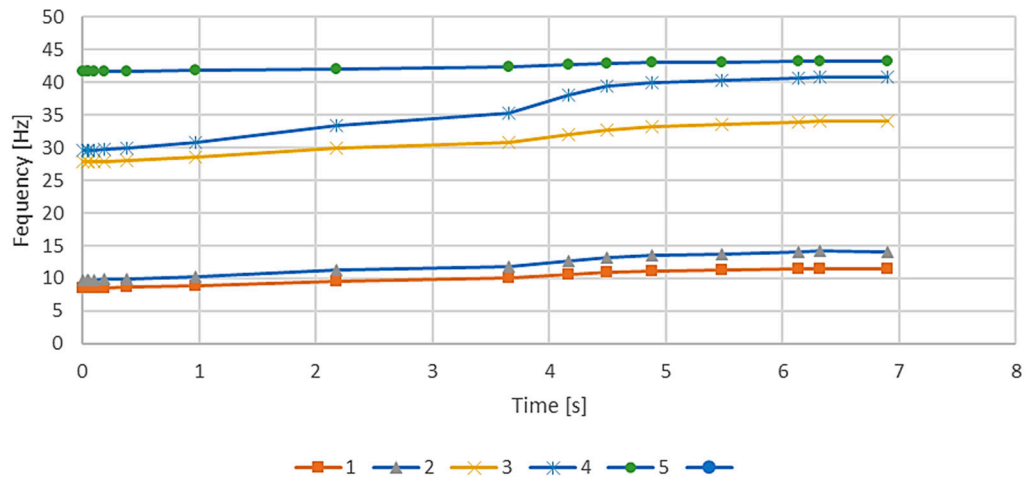


Figure 33. Rocket time-frequency graph with varying mass.

### 3.8.3. Time-Varying Fuel Model Derivation

In reference to Figures 34 and 35, we can see that the frequency of each mode incrementally changes with the changes in mass and the location of the centre of mass. The corresponding change in the mode shape is quantified using a modal correlation factor  $R$ , which is found by:

$$R(N_i) = N_i^0 \cdot N_i^k \tag{52}$$

where 0 denotes the initial, full-mass condition and  $k$  denotes a discrete timestep.  $R$  returns a value of 1 if the eigenmodes are parallel and 0 if they are orthogonal. We can plot the correlation factor for each mode as a function of time to discover how large the mode shape changes are.

Modes 1 to 3 have very little variation with changing fuel mass; however, modes 4 and 5 vary significantly. These modes are high-order bending forward of the centre of gravity, so it is evident that these modes are highly dependent on the location of the centre of gravity.

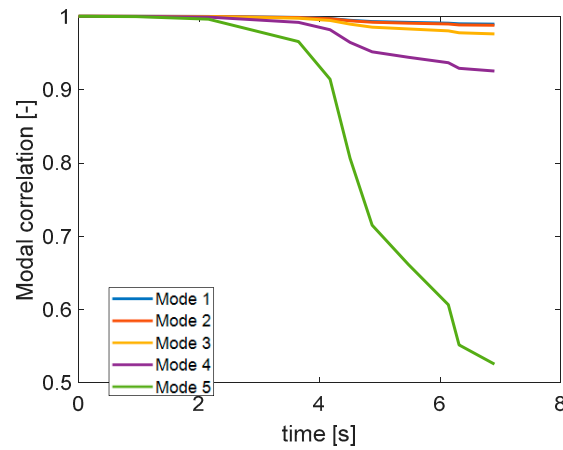


Figure 34. Modal correlation with burn time.

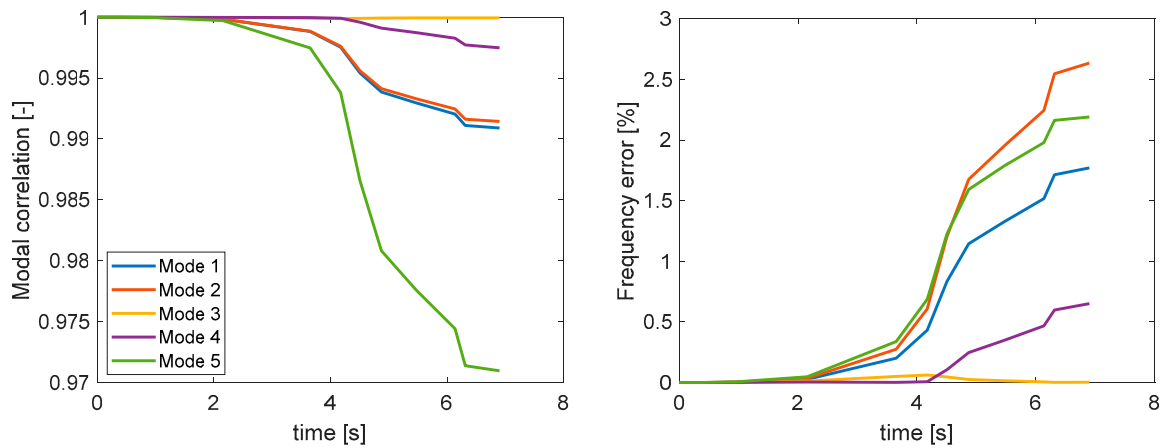


Figure 35. Modal correlation between time-varying SVD method and the eigenmodes (left) and the natural frequency error (right).

In the application of the method outlined in Equations (34)–(45) for this case study, we can find the variation between the instantaneous SVD method and the eigenmodes over time.

From this figure, we can conclude that the SVD method sufficiently characterises the change in the mode shape and frequency, with a minimum modal correlation of approximately 0.97 and a maximum frequency error of approximately 2.6%.

### 3.8.4. Modal Extraction

The aeroelastic deformation of the rocket was calculated under several different representative loading conditions. Figure 36 displays an example of the deformation of the rocket with a scale factor of 50. This figure clearly shows the mode shape of the rocket as well as the fact that the point of maximum displacement is at the nosecone.

The deflection of the nosecone (DOF 788 in the structural model) can be displayed under various loading conditions. First, the deflection of the nosecone without any pressures applied can be found (Figure 37). This is representative of the deformation solely due to the natural frequency and mode shapes of the rocket.

The deflection of the nosecone tip at Mach 0.5 with the applied pre-stress pressures can then be found, as shown in Figure 38. This figure displays the deflection of the nosecone over the time of the fuel burn, and convergence of the deflection is clearly seen. We also note a great increase in the magnitude of the deflection from approximately  $6 \times 10^{-7}$  m to  $4.75 \times 10^{-4}$  m.



**Figure 36.** Representation of deflected rocket at a scale factor of 50.

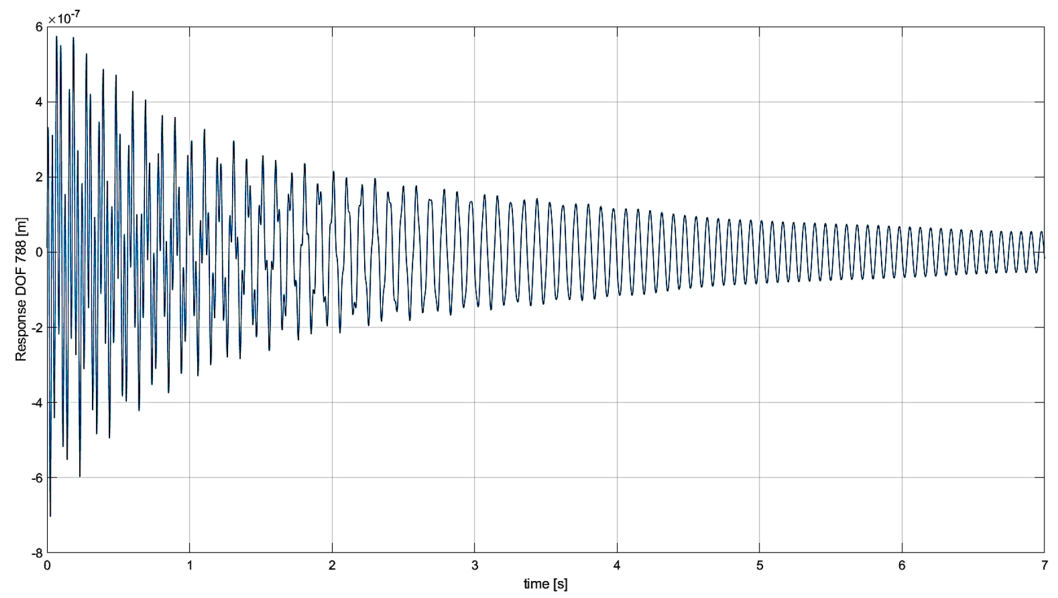


**Figure 37.** Nosecone deflection without loading.

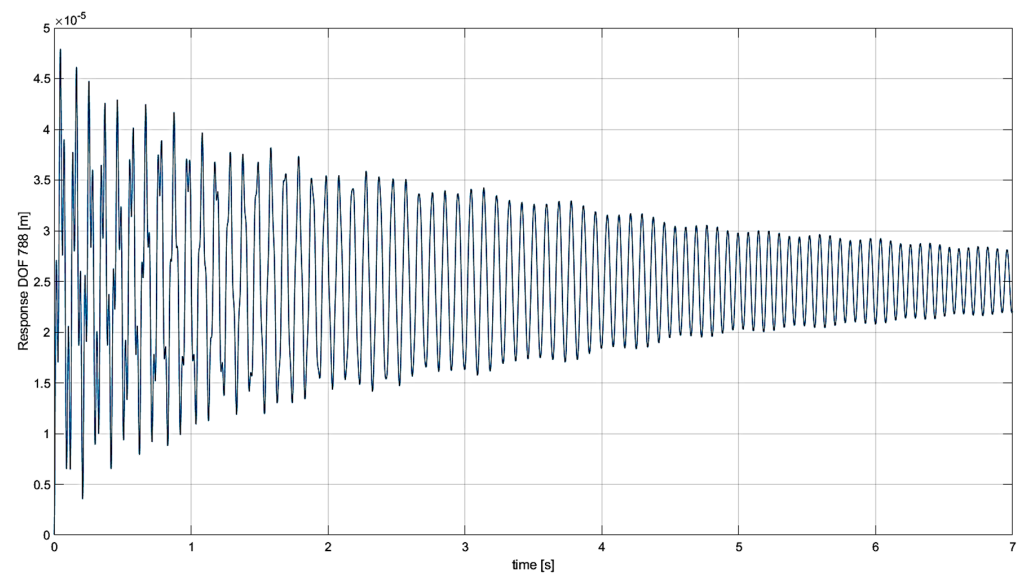


**Figure 38.** Deflection of nosecone under Mach 0.5 and pre-stress load.

The aeroelastic derivatives can then be applied to the deflection, as shown in Figure 39.

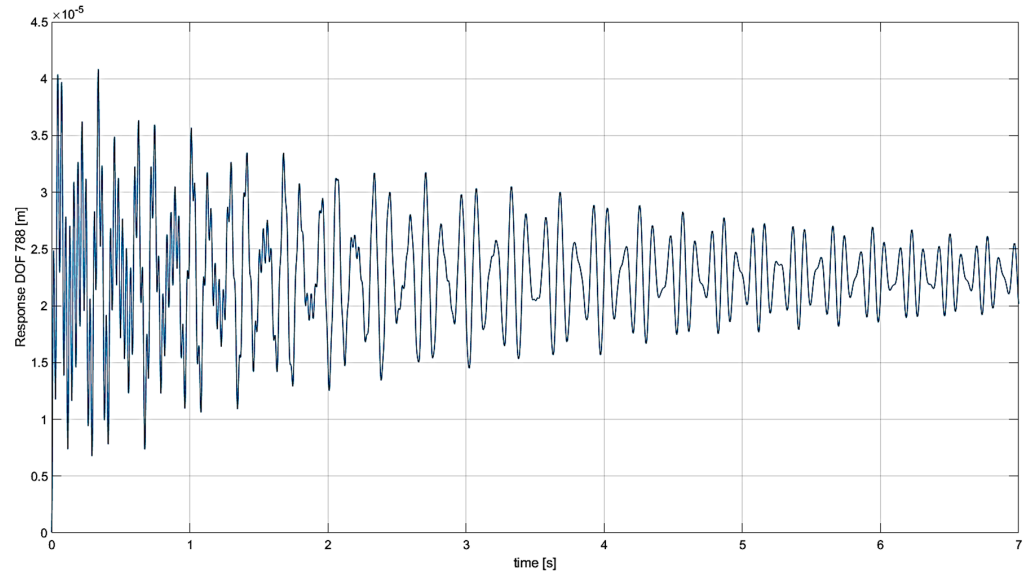


Figure 39. Nosecone deflection at Mach 0.5 with aeroelastic derivatives.

Figure 40 shows the interaction of the aerodynamic and structural forces. The frequency of the deflection is noticeably different to that given previously. The maximum deflection of the nosecone is only slightly reduced (from  $4.75 \times 10^{-4}$  m to  $4.0 \times 10^{-4}$  m) when compared to the case without the aeroelastic derivatives applied. Finally, we can plot the deflection of the nosecone over the range of Mach numbers from 0.3 to 2.2 under linear acceleration (Figure 40).

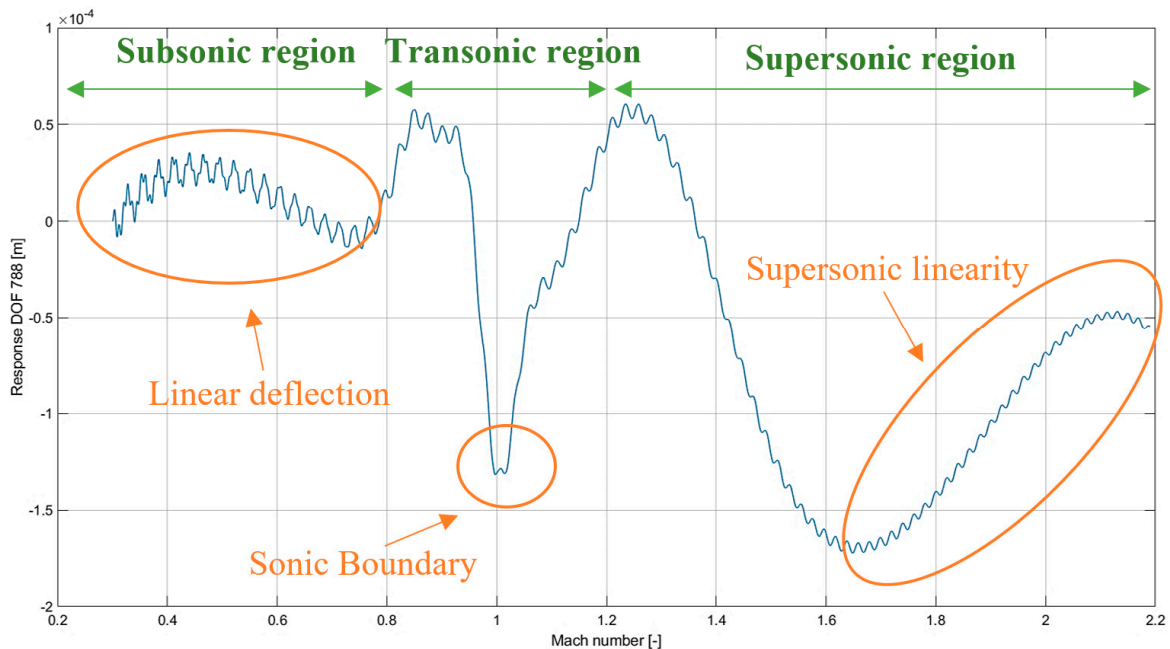


Figure 40. Deflection of the nosecone with respect to the Mach number with annotated regions and specific regimes.

As evident in the figure, there is a noticeable change in the deflection of the rocket as it moves from the subsonic regime into the transonic regime, and from the transonic regime into the supersonic regime. The subsonic regime is characterised by a regular sinusoidal change in the displacement of the nosecone tip. In this region, the deflection

in the DOF is very low, with a maximum displacement of approximately  $0.4 \times 10^{-4}$  m, or 0.4 mm. Entering the transonic region, the displacement in the DOF changes drastically, increasing from Mach 0.8–0.95 to  $0.55 \times 10^{-4}$  m before dropping sharply to  $-1.25 \times 10^{-4}$  m at the sonic boundary. This change is mirrored after the sonic boundary, rising back to  $0.55 \times 10^{-4}$  m as the rocket exits the transonic regime. The deflection of the nosecone as the rocket moves further into the supersonic regime shows a large negative deflection before beginning to return to a more sinusoidal deflection cycle, similar to the subsonic regime.

Here, we note that the absolute magnitude of the deflection remains very small when compared to the length of the rocket. In this case study, a maximum deflection of approximately  $-1.75 \times 10^{-4}$  m has been found, which is extremely small when compared to both the length (2.941 m) and diameter (0.131 m) of the rocket. This means that it is very unlikely that there will be large changes in the aerodynamic characteristics of the structure for the mission design selected, given the low angles of attack and sideslip angles developed. However, these effects may become more apparent for a similar rocket design that is able to be controlled (e.g., a surface-to-air missile) as the control inputs could result in much larger aerodynamic forces and thus larger deflections.

#### 4. Conclusions

This article has presented a tailored methodology for the derivation of high-fidelity dynamics models for sounding rockets, incorporating the aeroelastic response of the platform in the relevant flight regimes, as well as realistic perturbations and parachute deployment effects. The adopted time-varying method provides a means to calculate the rocket deformation characteristics throughout the flight due to flow-structure interactions and as a function of both environmental conditions and fuel burn. This supports the development of a fully-aeroelastic flight simulation, significantly increasing the accuracy of the trajectory prediction for design and verification purposes. The proposed method is generalisable to the design of many aerospace vehicles and, thus, holds good potential for future developments, tailoring and extensions. More specifically, the proposed methodology lays foundations for the development of both offline and online digital twins, which can be used to predict/reconstruct the accurate flight trajectory and the effects of the aerodynamic loading on the aeroelastic response of the rocket. In a real-time implementation, the digital twin can also compensate for temporary faults of the rocket's navigation sensors and support the development of model-predictive control logics for highly-automated flight guidance systems.

Further research is necessary to address aspects that were left outside the scope of this project, such as using real weather data and modelling the effects of motor vibration on the vehicle dynamics. Furthermore, a transient aeroelastic solver could improve the ability to capture additional structural response effects, which may be generated by unstable shockwaves or by very large angles of attack. Additionally, adaptive meshing methods will be used in the future to improve the computational performance of the aeroelastic analysis tools. In terms of atmospheric modelling, while our proposed approach (i.e., 1-cosine discrete gust and von Karman continuous turbulence models) is theoretically superior to other published methodologies, there remain some inherent limitations limiting its applicability to all possible weather conditions.

The future experimental validation of the developed high-fidelity model will include a detailed comparison between the model predictions and real flight test data. Following such experimental phase, the first real-time implementation of the proposed high-fidelity multi-physics model will be in the form of a virtual (i.e., fully digital) navigation sensor, compensating for the errors and shortcomings of onboard (i.e., physical) navigation sensors and systems. Additionally, the possibility of using physics-based Artificial Intelligence (AI) for the development and real-time integration of digital twins in various aerospace vehicles will be investigated. These efforts will focus on both high-integrity navigation sensors and trusted autonomous flight guidance systems for various platforms, including rockets, drones and reusable space vehicles for point-to-point suborbital transport.

**Author Contributions:** Conceptualization and methodology: all authors contributed; investigation, software and resources: S.S., B.M. and R.C.; validation: A.G., R.C. and R.S.; writing—original draft preparation: B.M., S.S.; writing—review and editing: A.G. and R.S.; supervision: R.S. and A.G. All authors have read and agreed to the published version of the manuscript.

**Funding:** This research received no external funding.

**Data Availability Statement:** Data available upon request to the authors, noting that some of the datasets are very large in size so clarifications regarding the needs and purposes are highly recommended.

**Acknowledgments:** The authors gratefully acknowledge the work of the RMIT HIVE rocket team in the design and manufacturing of the Ad Astra II rocket and their provision of design specifications and support through this project.

**Conflicts of Interest:** The authors declare no conflict of interest.

## References

1. Bijjahalli, S.; Sabatini, R.; Gardi, A. Advances in intelligent and autonomous navigation systems for small UAS. *Prog. Aerosp. Sci.* **2020**, *115*, 100617. [CrossRef]
2. Gardi, A.; Sabatini, R.; Kistan, T. Multiobjective 4D Trajectory Optimization for Integrated Avionics and Air Traffic Management Systems. *IEEE Trans. Aerosp. Electron. Syst.* **2018**, *55*, 170–181. [CrossRef]
3. Ramasamy, S.; Sangam, M.; Sabatini, R.; Gardi, A. Flight Management System for Unmanned Reusable Space Vehicle Atmospheric and Re-Entry Trajectory Optimisation. *Appl. Mech. Mater.* **2014**, *629*, 304–309. [CrossRef]
4. Cappello, F.; Bijjahalli, S.; Ramasamy, S.; Sabatini, R. Aircraft Dynamics Model Augmentation for RPAS Navigation and Guidance. *J. Intell. Robot. Syst. Theory Appl.* **2017**, *91*, 1–15.
5. Cappello, F.; Ramasamy, S.; Sabatini, R. A low-cost and high performance navigation system for small RPAS applications. *Aerosp. Sci. Technol.* **2016**, *58*, 529–545. [CrossRef]
6. Sabatini, R.; Moore, T.; Hill, C. A New Avionics-Based GNSS Integrity Augmentation System: Part 1—Fundamentals. *J. Navig.* **2013**, *66*, 363–384. [CrossRef]
7. Sabatini, R.; Moore, T.; Hill, C. A New Avionics-Based GNSS Integrity Augmentation System: Part 2—Integrity Flags. *J. Navig.* **2013**, *66*, 501–522. [CrossRef]
8. Sabatini, R.; Moore, T.; Hill, C. Avionics-based GNSS integrity augmentation synergies with SBAS and GBAS for safety-critical aviation applications. In Proceedings of the 2016 IEEE/AIAA 35th Digital Avionics Systems Conference (DASC), Sacramento, CA, USA, 25–29 September 2016; pp. 1–10. [CrossRef]
9. Ranasinghe, K.; Sabatini, R.; Gardi, A.; Bijjahalli, S.; Kapoor, R.; Fahey, T.; Thangavel, K. Advances in Integrated System Health Management for mission-essential and safety-critical aerospace applications. *Prog. Aerosp. Sci.* **2021**, *128*, 100758. [CrossRef]
10. Hilton, S.; Cairola, F.; Gardi, A.; Sabatini, R.; Pongsakornsathien, N.; Ezer, N. Uncertainty Quantification for Space Situational Awareness and Traffic Management †. *Sensors* **2019**, *19*, 4361. [CrossRef] [PubMed]
11. Bolz, R.E.; Nicolaides, J.D. A method of determining some aerodynamic coefficients from supersonic free-flight tests of a rolling missile. *J. Aeronaut. Sci.* **1950**, *17*, 609–621. [CrossRef]
12. Chusilp, P.; Charubhun, W.; Nutkumhang, N. A comparative study on 6-DOF trajectory simulation of a short range rocket using aerodynamic coefficients from experiments and missile DATCOM. In Proceedings of the 2nd TSME International Conference on Mechanical Engineering, Nonthaburi, Thailand, 19–21 October 2011; pp. 19–21.
13. Chowdhury, S.; de La Beaujardiere, J.P.; Brooks, M.; Roberts, L. An Integrated Six Degree-of-Freedom Trajectory Simulator for Hybrid Sounding Rockets. In Proceedings of the 49th AIAA Aerospace Sciences Meeting including the New Horizons Forum and Aerospace Exposition, Orlando, FL, USA, 4–7 January 2011. [CrossRef]
14. Roshanian, J.; A Bataleblu, A.; Ebrahimi, M. Robust ascent trajectory design and optimization of a typical launch vehicle. *Proc. Inst. Mech. Eng. Part C: J. Mech. Eng. Sci.* **2018**, *232*, 4601–4614. [CrossRef]
15. Rosema, C.; Doyle, J.; Auman, L.; Underwood, M.; Blake, W.B. Missile DATCOM User’s Manual-2011 Revision. 2008. Available online: <https://www.semanticscholar.org/paper/MISSILE-DATCOM-User%27s-Manual-2011-Revision-Rosema-Doyle/0190147a0905ea452d7fa36d0d663044aa5f460a> (accessed on 12 February 2022).
16. Moore, F.G.; Moore, L.Y. 2009 Version of the Aeroprediction Code: AP09. *J. Spacecr. Rocket.* **2008**, *45*, 677–690. [CrossRef]
17. Escalante, J.F.G.; Xu, R.; Ogawa, H.; Pudsey, A. CFD-coupled 6-DOF attitude and trajectory analysis for hypersonic air vehicles. In Proceedings of the Australian International Aerospace Congress, Avalon, Australia, 1 January 2019; p. 64.
18. Sahu, J. Time-accurate numerical prediction of free-flight aerodynamics of a finned projectile. *J. Spacecr. Rocket.* **2008**, *45*, 946–954. [CrossRef]
19. Li, H.; Ye, Z. Numerical investigation on aerodynamic and inertial couplings of flexible spinning missile with large slenderness ratio. *Aerosp. Sci. Technol.* **2020**, *99*, 105582. [CrossRef]
20. Meyers, S. Aeroelastic analysis of sounding rocket vehicles. In Proceedings of the 3rd Sounding Rocket Technology Conference, Albuquerque, NM, USA, 7–9 March 1973. [CrossRef]

21. Arbic, R.G.; White, G.; Gillespie, J.W. *Some Approximate Methods for Estimating the Effects of Aeroelastic Bending of Rocket-Propelled Model-Booster Combinations*. Confidential Report AD-5160 (Declassified); NASA Langley: Hampton, VA, USA, 1953.
22. Smith, T.E. *A Modal Aeroelastic Analysis Scheme for Turbomachinery Blading*; NASA Contract Report CR-187089: Cleveland, OH, USA, 1991.
23. Abbas, L.K.; Chen, D.; Rui, X. Numerical Calculation of Effect of Elastic Deformation on Aerodynamic Characteristics of a Rocket. *Int. J. Aerosp. Eng.* **2014**, *2014*. [[CrossRef](#)]
24. Lindhorst, K.; Haupt, M.C.; Horst, P. Aeroelastic Analyses of the High-Reynolds-Number-Aerostructural-Dynamics Configuration Using a Nonlinear Surrogate Model Approach. *AIAA J.* **2015**, *53*, 2784–2796. [[CrossRef](#)]
25. Hua, R.; Ye, Z.; Wu, J. Effect of elastic deformation on flight dynamics of projectiles with large slenderness ratio. *Aerosp. Sci. Technol.* **2017**, *71*, 347–359. [[CrossRef](#)]
26. Joseph, N.; Carrese, R.; Marzocca, P. A Physics-Based Projection Algorithm for Fluid Structure Interaction Simulations. In Proceedings of the AIAA Scitech 2019 Forum, San Diego, Ca, USA, 7–11 January 2019. [[CrossRef](#)]
27. Tihomirov, D.; Raveh, D.E. Nonlinear Aerodynamic Effects on Static Aeroelasticity of Flexible Missiles. In Proceedings of the AIAA Scitech 2019 Forum, San Diego, Ca, USA, 7–11 January 2019. [[CrossRef](#)]
28. US Department of Defense. *Global Climactic Data for Developing Military Products*; Department of Defense Handbook MIL-HDBK-310: Washington, DC, USA, 1997.
29. Wu, Z.; Cao, Y.; Ismail, M. Gust loads on aircraft. *Aeronaut. J.* **2019**, *123*, 1216–1274. [[CrossRef](#)]
30. Moorhouse, D.J.; Woodcock, R.J. *Background Information and User Guide for MIL-F-8785C, Military Specification-Flying Qualities of Piloted Airplanes*; Air Force Labs Wright-Patterson AFB OH: Dayton OH, USA, 1982.
31. US Department of Defense. *Flying Qualities of Piloted Aircraft*; US Department of Defense Handbook MIL-STD-1797A: Washington, DC USA, 1997.
32. Reimer, L.; Heinrich, R.; Ritter, M. Towards Higher-Precision Maneuver and Gust Loads Computations of Aircraft: Status of Related Features in the CFD-Based Multidisciplinary Simulation Environment FlowSimulator. In *Notes on Numerical Fluid Mechanics and Multidisciplinary Design Book Series*; Springer: Cham, Switzerland, 2019; pp. 597–607. [[CrossRef](#)]
33. Bekemeyer, P.; Thormann, R.; Timme, S. Rapid gust response simulation of large civil aircraft using computational fluid dynamics. *Aeronaut. J.* **2017**, *121*, 1795–1807. [[CrossRef](#)]
34. Justus, C.G.; Campbell, C.W.; Doubleday, M.; Johnson, D.L. *New Atmospheric Turbulence Model for Shuttle Applications*; NASA Technical Memorandum TM-4168, NASA George C. MarsbalZ Space Flight Center Marshal Space Flight Center: Huntsville, AL, USA, 1990.
35. Johnson, D.L.; Vaughan, W.W. The Role of Terrestrial and Space Environments in Launch Vehicle Development. *J. Aerosp. Technol. Manag.* **2019**, *11*, e4719. [[CrossRef](#)]
36. Maydew, R.C.; Peterson, C.W.; Orlik-Rueckemann, K.J. *Design and Testing of High-Performance Parachutes (la Conception et les Essais des Parachutes a Hautes Performances)*; NATO Advisory Group for Aerospace Research and Development (AGARD): Neuilly-Sur-Seine, France, 1991.
37. Cheng, H.; Yu, L.; Rong, W.; Jia, H. A numerical study of parachute inflation based on a mixed method. *Aviation* **2012**, *16*, 115–123. [[CrossRef](#)]
38. Sudars, M.; Wong, H.; Barrio, A.M. EXPERT 6-DoF Entry Trajectory Analysis including flight under parachute simulations. In Proceedings of the 4th International Conference on Astrodynamics Tools and Techniques (ICATT), Madrid, Spain, 3–6 May 2010; pp. 3–6.
39. Deacon, S. *Development, Verification, and Future Applications of a 3-DOF Entry and Descent Simulation Tool*; ProQuest Dissertations Publishing: Ann Arbor, MI, USA, 2008.
40. Hanson, J.M.; Beard, B.B. Applying Monte Carlo simulation to launch vehicle design and requirements verification. *J. Spacecr. Rocket.* **2012**, *49*, 136–144. [[CrossRef](#)]
41. Eerland, W.J.; Box, S.; Fangohr, H.; Söbester, A. An open-source, stochastic, six-degrees-of-freedom rocket flight simulator, with a probabilistic trajectory analysis approach. In Proceedings of the AIAA Modeling and Simulation Technologies Conference, Grapevine, TX, USA, 9–13 January 2017; p. 1556.
42. Roshanian, J.; Bataleblu, A.; Ebrahimi, M. A novel metamodel management strategy for robust trajectory design of an expendable launch vehicle. *Proc. Inst. Mech. Eng. Part G: J. Aerosp. Eng.* **2019**, *234*, 236–253. [[CrossRef](#)]
43. Public Domain. (2020, 14/06/20). ECEF. Available online: <https://en.wikipedia.org/wiki/ECEF> (accessed on 12 February 2022).
44. Siouris, G.M. *Missile Guidance and Control Systems*; Springer Science & Business Media: Berlin, Germany, 2004.
45. AUTODESK. (2019, 12/06/2020). SST K-Omega Turbulence Models. Available online: <https://knowledge.autodesk.com/support/cfd/learn-explore/caas/CloudHelp/cloudhelp/2014/ENU/SimCFD/files/GUID-0F5C4828-9F91-46B6-A16A-2578D72DCFCC-htm.html> (accessed on 12 February 2022).
46. Macha, J. A simple, approximate model of parachute inflation. In Proceedings of the Aerospace Design Conference, Irvine, CA, USA, 16–19 February 1993.
47. Pratap, M.; Agrawal, A.K.; Kumar, S. Design and Selection Criteria of Main Parachute for Re entry Space Payload. *Def. Sci. J.* **2019**, *69*, 531–537. [[CrossRef](#)]
48. RMIT HIVE. “Australian Universities Rocket Competition (AURC) Progress Report 2”, Protected Competition Design Document, Excerpts Available Upon Motivated Request to the Authors; RMIT University: Bundoora, VIC, Australia, 2020.

49. AZO Materials. (2020, 09/02/2020). S-Glass Fibre. Available online: <https://www.azom.com/properties.aspx?ArticleID=769> (accessed on 12 February 2022).
50. Sutton, G.P.A.; Biblarz, O. *Rocket Propulsion Elements*, 9th ed.; Wiley: Hoboken, NJ, USA, 2017.
51. ASM. (2020, 09/02/2020). Available online: <http://asm.matweb.com/search/SpecificMaterial.asp?bassnum=MA6061T6> (accessed on 12 February 2022).
52. Han RP, S.; Bainum, P.M.; Zheng, Z.C.; Guo, D.; Zhang, Y.J.; Hou, Z.C. Dynamic analysis of large-scale flexible systems for free—Free space structures. *Philos. Trans. R. Soc. London. Ser. A Math. Phys. Eng. Sci.* **2001**, 359, 2209–2229.

**Disclaimer/Publisher’s Note:** The statements, opinions and data contained in all publications are solely those of the individual author(s) and contributor(s) and not of MDPI and/or the editor(s). MDPI and/or the editor(s) disclaim responsibility for any injury to people or property resulting from any ideas, methods, instructions or products referred to in the content.